The International Journal of Advanced Manufacturing Technology (2021) 116:175–195
https://doi.org/10.1007/s00170-021-07346-2

ORIGINAL ARTICLE

Simulation of the chip morphology together with its evolution in machining of Inconel 718 by considering widely spread cutting speed

Chun Liu[1,2] · Min Wan[1,2] · Yun Yang[1,2]

Received: 30 November 2020 / Accepted: 25 May 2021 / Published online: 15 June 2021

Abstract
This article establishes a finite element method (FEM) model to characterize and classify the chip morphologies of Inconel 718, which tends to form shear localized chips. Orthogonal cutting simulations in a wide range of speeds with three uncut chip thicknesses are carried out to model the plastic deformation of Inconel 718 and thus the formation of the serrated chips by utilizing the Johnson-Cook (JC) constitutive law with the criterion of the accumulated plastic strain. Evolution trends of the chip deformation results are of the main interest and focus is placed on the chip segmentation. Simulation results show that Inconel 718 exhibits a chip pattern transition from the continuously smooth form to the regularly serrated form with the increase of cutting speed. However, the disappearance of chip serration is also observed at still higher cutting speeds. The primary shear angle and the segment inclination finally reach the same asymptotic value of 45°. The shear band spacing drops significantly before the two plateau regions are achieved. Apart from these, the scatter plot of specific cutting force tends to be a concave shape, while the scatter plot of chip segmentation degree tends to be a convex shape. Meanwhile, the chip thickness ratio approaches an asymptotic value, and the average velocity of chip sliding on the tool rake face almost equals the cutting speed. At the same time, the simulation results are compared to the results by experiments or simulations in the published literatures. Moreover, the FEM model is validated by comparing the chip morphologies from the experiments and the simulations, respectively. The proposed work is fundamental for not only increasing understandings of the metal cutting process of Inconel 718, but also hypothetically providing a framework of the chip generation under the cutting speed from low to high range.

Keywords Inconel 718 · Cutting simulation · Serrated chip · Chip morphology

1 Introduction

Nickel-based superalloys are widely used in the hot sections of aircraft engines for critical components such as vanes, discs and liners in gas turbines, mainly because of their excellent mechanical strength at elevated temperatures, resistance to wear and chemical degradation [1]. Among the nickel-based superalloys, Inconel 718 is well known and considered as an extremely difficult-to-cut material [2–4]. As reported in Ref. [5], the relative machinability (feed rate) of Inconel 718 was about $\frac{1}{16}$ of aluminum alloy, $\frac{1}{6}$ of mild steel and $\frac{1}{4}$ of stainless steel, respectively. Besides, it is noted in Refs. [6, 7] that the range of cutting speeds for high speed milling of nickel-based alloys was about 50 m/min $\sim$ 600 m/min, which was the lowest high speed milling range when compared to those of titanium, steel, cast iron, bronze brass, aluminum and fiber reinforced plastics. Poor machinability of Inconel 718 is often due to its low thermal conductivity, high toughness, work hardening behavior and chemical affinity for most tool materials [5, 8, 9]. These features cause the alloy's milling, drilling and turning at much lower cutting speeds and feeds. Therefore, practical machining of Inconel 718 to achieve favorable metal parts usually needs more time and higher cost.

✉ Min Wan
m.wan@nwpu.edu.cn

[1] School of Mechanical Engineering, Northwestern Polytechnical University, Xi'an, Shaanxi, 710072, China

[2] State IJR Center of Aerospace Design and Additive Manufacturing, Northwestern Polytechnical University, Xian, Shaanxi, 710072, China

When machining nickel alloys is concerned, the growing demand for high production efficiency has prompted continuous research of excellent cutting tool materials and machining methods. One progress that can improve the machinability of nickel alloys is the development of high speed machining technology, which has advantages of high metal-removal rate with low cutting force, good machining accuracy and sound surface finish [3, 10]. The machining characteristics and the chip morphologies of Inconel 718 under conventional cutting speeds have been studied extensively. However, the range of very high cutting speeds is still largely unexploited. The main reason is that high cutting speed also encourages the emergence of highly serrated chips [11], which usually leads to cutting instability correlated with increased tool wear, degraded surface finish and reduced machining accuracy [12].

Another progress is that finite element softwares have been developed to help simulate a particular machining operation in the computational environment. It not only promotes better understanding of the cutting process but also saves time and money in generating reasonable solutions, like obtaining optimal cutting parameters. Finite element analysis was firstly applied to study mental cutting process in the early 1970s when Tay et al. [13] developed a two-dimension (2D) FEM model for the orthogonal turning of a free-machining steel in order to determine the temperature distribution in chip and cutting tool. Since then, two and three dimensional simulations of machining have been developed. Through FEM simulations, a rich set of variables such as the fields of strain, stress and temperature [14] can be obtained to predict the material deformation characteristics and the machining performance. Parameters such as cutting speeds and feeds can directly influence chip morphology, cutting force and other quantities related to the chip formation process. Thus, many investigators have developed various analytical and numerical models to comprehend the features that relate to the chip formation process.

One of the main characteristics in machining of Inconel 718 is to produce the serrated or the segmented chips, which involve large strains, high strain rates and high temperatures, in a wide range of cutting speeds and feeds. Existing studies show that on the one hand, the chip serration or segmentation by shear localization affects the machined surface integrity. On the other hand, the serrated or the segmented chips by shear localization are easy to break, and this contributes to the chip's evacuation and disposal [15], and thus the automation of machining operations and other applications involving chip recycling [16, 17]. Actually, shear localized bands, from a few micrometers to a few tens of micrometers wide [18] observed within the serrated chips, are alternately separated by segment bulks [19]. With poor thermal properties, the generated heats are concentrated, and further increase the local temperature to a high value since the heat diffusion does not have enough time to smooth the temperature field. Then adiabatic shearing happens where plastic deformation is highly intense [20]. Consequently, materials in the shear zones are subject to thermal softening and rapid deformation [21], and they in turn contribute to strain localization and temperature rising. Thus, cutting simulations to understand the chip formation mechanism of Inconel 718 is vital for machining this alloy effectively and efficiently. Much work needs to be done to analyze the serrated chip formation mechanism of Inconel 718 that covers onset, propagation and interaction of adiabatic shear bands.

Chip formation in machining plays an important role in the cutting process, and chip morphology often reflects the choice of cutting conditions [22]. In this work, a FEM model is established to explore the serrated chip formation mechanism and the chip morphology evolution of Inconel 718. Orthogonal cutting simulations are conducted by combining a wide range of cutting speeds. It is useful to grasp the details that involve in the chip formation process, and this cannot be easily obtained by actual cutting operations. The proposed work is as follows. First, descriptions of the FEM model employed for the orthogonal cutting simulations are given. Second, simulations are conducted to collect the generated chips and the cutting forces. Third, results obtained from the orthogonal cutting simulations are quantitatively analyzed, and experiments are designed and conducted to validate the FEM model. Finally, overall conclusions are summarized.

2 Numerical modeling

2.1 Basic simulation procedure

Various FEM simulations have been developed to study the cutting response of different metals and alloys. In this work, the Johnson-Cook (JC) model [23], which is a strain rate- and temperature-dependent viscoplastic material model suitable for materials subject to large strains, high strain rates and high temperatures, is adopted. The von Mises tensile flow stress, i.e., σ, involved in the model is expressed as follows [23].

$$\sigma = \left(A + B\varepsilon^{n}\right)\left[1 + C\ln\left(\frac{\dot{\varepsilon}}{\dot{\varepsilon}_0}\right)\right]\left[1 - \left(\frac{T - T_0}{T_m - T_0}\right)^{m}\right] \quad (1)$$

where the equivalent plastic strain ε is expressed as $\varepsilon = \int \dot{\varepsilon}\, dt$ with $\dot{\varepsilon}$ being the equivalent plastic strain rate with respect to the reference plastic strain rate $\dot{\varepsilon}_0$. T is the current material temperature in Kelvin. T_0 is the reference temperature. T_m is the material melting temperature. It

Table 1 Johnson-Cook (JC) constitutive model parameters for Inconel 718 [24]

A [MPa]	B [MPa]	n	C	m	$\dot{\varepsilon_0}$ [s^{-1}]	T_0 [K]	T_m [K]
1350	1139	0.65	0.014	1.0	1.0	300	1570

should be pointed out that the items appearing in the first, the second and the third brackets describe the effects of the strain hardening, the strain rate hardening and the thermal softening in the plastic flow, respectively.

In this study, evolution trends of the chip deformation results are of the main interest, and focus is placed on the chip segmentation. Therefore, emphasis is not put on modifications and improvements of the JC constitutive law, and the existing one, i.e., Eq. (1), is used in the study. For Inconel 718, the basic parameters required in the JC model together with the main physical and mechanical property parameters, are taken from the work reported in Ref. [24], as listed in Tables 1 and 2. The main physical and mechanical property parameters of the tool used for simulations is taken from the Ref. [14], as listed in Table 2. The fraction of inelastic heat β used in the FEM simulations is treated as a constant of 0.9 for considering the heat generation rate due to the work of the plastic deformation of Inconel 718.

To well simulate how the elements of the workpiece material separate to form the chip and the machined surface, one of the most important aspects is damage and separation principle, such as node separation, element deletion and adaptive remeshing [25]. There are two criteria, which are widely used to describe the separation between chip and workpiece matrix. The first is the geometric criterion [26, 27], and the second are physical criteria [28–30]. The former uses a critical distance, which is defined as the length between the tool tip on the cutting path and the unit node in front of the tool tip, to judge whether it reaches the preset critical failure value. Once the distance reaches the preset critical failure value, the node will fracture and separate into two nodes. One will continue to flow with the formed chip, and the other node will remain on the machined surface. The latter takes the equivalent plastic strain, fracture stress, strain energy density or other physical variables as the criterion for chip separation from workpiece matrix [30]. That is, as long as the physical variables at the tool tip reach the preset critical value, the unit nodes are separated.

Table 2 Physical and mechanical properties of Inconel 718 [24] and tool [14]

Parameter	Inconel 718	Tool
Mass density ρ [kg m^{-3}]	8200	15000
Modulus of elasticity E [GPa]	210	800
Poisson's coefficient υ	0.3	0.2
Heat conductivity k [W m^{-1} K^{-1}]	11.4	46
Thermal expansion α [μm m^{-1} K^{-1}]	12.0	4.7
Specific heat capacity C_p [J kg^{-1} K^{-1}]	435	203

In this work, a damage criterion is used based on the accumulated plastic strain. The material element is assumed to be undamaged from the surrounding elements when the accumulated value ε is smaller than the critical value ε_{crit}, and it is totally damaged when ε reaches ε_{crit}. Here, it should be pointed out that the critical strain is used to avoid excessive mesh distortion in the finite element computation, and this damage criterion was previously proved to be effective in predicting the failure of ductile materials subject to high loading rates in different situations [31, 32]. In this work, fracture is controlled by ε_{crit} and can be triggered by the high level of plastic localized strain within shear bands.

In order to analyze and clarify the link between the adiabatic shearing, the chip morphology and the cutting conditions, a plane strain model of orthogonal cutting is developed using the finite element with Lagrangian formulation. The basic geometry of the numerical model and the 2D-FEM model for orthogonal cutting process are shown in Fig. 1. The workpiece is considered as plastic material whereas the cutting tool is treated here for simplicity as a rigid body. The heat conductions between the workpiece matrix, the tool surface and the chip have been considered and thus set in the cutting simulations.

A sharp tool is considered and only one degree of freedom along the cutting direction is allowed. The cutting speed V_c is applied to the reference point (RP) on the tool right-top corner. Mechanical boundary conditions are defined to fix the workpiece at the bottom and the two sides, and it means no rotational or translational degrees of freedom. The tool rake angle α and the tool clearance angle γ are set as 0° and 6°, respectively. The cutting speed V_c and the uncut chip thickness t_1 vary in different simulations. If V_c is larger than 10 m/s, the overall friction coefficient is very small [34], and its speed dependence is poorly known. For the convenience of study, the mechanical contact at the tool-chip interface is defined as a friction-free constraint for the large range of speeds explored.

The mesh of workpiece is divided into the three different zones with different mesh densities, namely, the uncut chip material (zone A), the fracture material (zone B) and the workpiece matrix (zone C). Finer meshes in zone A are used to capture the high level of strain localization in the narrow shear bands for better accuracy. The layers of material that will be removed by the cutting tool are comprised of zone A and zone B (thin joint layer of 5 μm in thickness). The upper limit of zone C corresponds to the machined surface. The meshes at zone B and zone C are parallel to horizontal and vertical directions, while the mesh at zone A is characterized by an inclination angle δ with the tool rake face. This

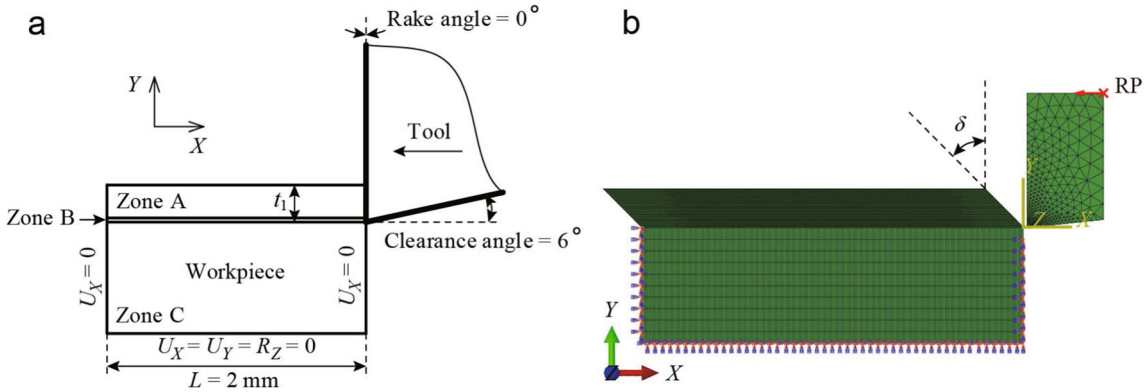

Fig. 1 **a** Orthogonal cutting configuration and decomposition of the workpiece material with three different zones [33]. **b** 2D-FEM model for orthogonal cutting process

orientation of mesh is aimed to facilitate the formation of the segmented chip flow during orthogonal cutting [24, 35–37]. An optimal mesh orientation $\delta = 45°$ reported in Refs. [24, 33] is adopted.

The shear damage parameter ε_{crit} is assigned to zone B. Up to failure, zone B behaves according to the JC model. No remeshing technique is used. The damage can evolve in a defined displacement D_{crit} and an element is deleted when $\varepsilon = \varepsilon_{crit}$, and it enables the chip to be separated from the workpiece matrix. It should be noted that ε_{crit} is the fracture strain for shear damage and D_{crit} is the displacement at failure for damage evolution. Therefore, fracture can propagate along the shear band where the plastic strain is localized.

2.2 Analysis of chip morphology

Orthogonal cutting simulations were conducted to analyzed the effects of various cutting speeds V_c under three uncut chip thicknesses (or depths of cut) t_1 on the adiabatic shear banding in the orthogonal cutting process. An idealized model for a regularly segmented chip along the tool rake face is illustrated in Fig. 2a. The serrated chip morphology can be characterized by the parameters of the maximum chip thickness $t_{c\_\max}$, the minimum chip thickness $t_{c\_\min}$, the shear band thickness δ_s, the spacing between neighboring shear bands L_s, the serrated chip pitch L_1, the segment inclination ϕ_{seg} and the shear angle ϕ_s (orientation of the primary shear zone). Besides these parameters, there are some other variables for chip morphology analysis. For instance, V_{chip} is the mean velocity of chip sliding on the tool rake face. V_s and V_{seg} represent the velocity discontinuity along shear planes.

A view of the segmented chip obtained from the orthogonal cutting simulation is shown in Fig. 2b. The segmented morphology shows that the chip is somehow continuous though it depicts a serrated pattern, according to the description and the subdivision of the continuous chips in Refs. [38, 39]. Concentrations of the plastic deformation (shear strain localization) are observed in Fig. 2b and c. Consequently, these deformations cause the irregularity of chip thickness and the fluctuation of cutting force.

The intensity of chip serration is characterized by the degree of segmentation, i.e., D_s, which is evaluated as follows [11, 40].

$$D_s = \frac{t_{c\_\max} - t_{c\_\min}}{t_{c\_\max}} \tag{2}$$

The shear angle ϕ_s and the segment inclination ϕ_{seg} are differentiated, as shown in Fig. 2a. The segment inclination ϕ_{seg} is the final orientation of shear bands, while the shear angle ϕ_s represents the orientation at the onset of shear banding similar to that describing shear orientation in the primary shear zone of a continuously smooth chip. Since the pattern of chip segmentation is not quite regular, the shear angle ϕ_s can be identified from the serrated chip simulated, as illustrated in Fig. 2c. That is, it is the average value of $\angle D_1D_2D_3$. $L_{s\_\max}$, $L_{s\_\min}$ and L_1 are the average lengths of A_1A_2, B_1B_2 and C_1C_2 measured along the chip segment, respectively.

The segment inclination ϕ_{seg} is related to L_s and L_1 and it can be calculated by

$$\phi_{seg} = \arccos\left(\frac{L_s}{L_1}\right) + \alpha \tag{3}$$

Since orthogonal cutting is considered in this work, $\alpha = 0°$ is used.

It is noted that the simulated chip morphology, as shown in Fig. 2b, is not as regular as that in Fig. 2a. The chip is divided into small segments by spaced shear bands. In fact, irregularities are observed in the serrated chip's thickness and shear bands are curved. The spacing L_s between neighboring shear bands near to the chip's free surface appears to be smaller than that near to the chip's

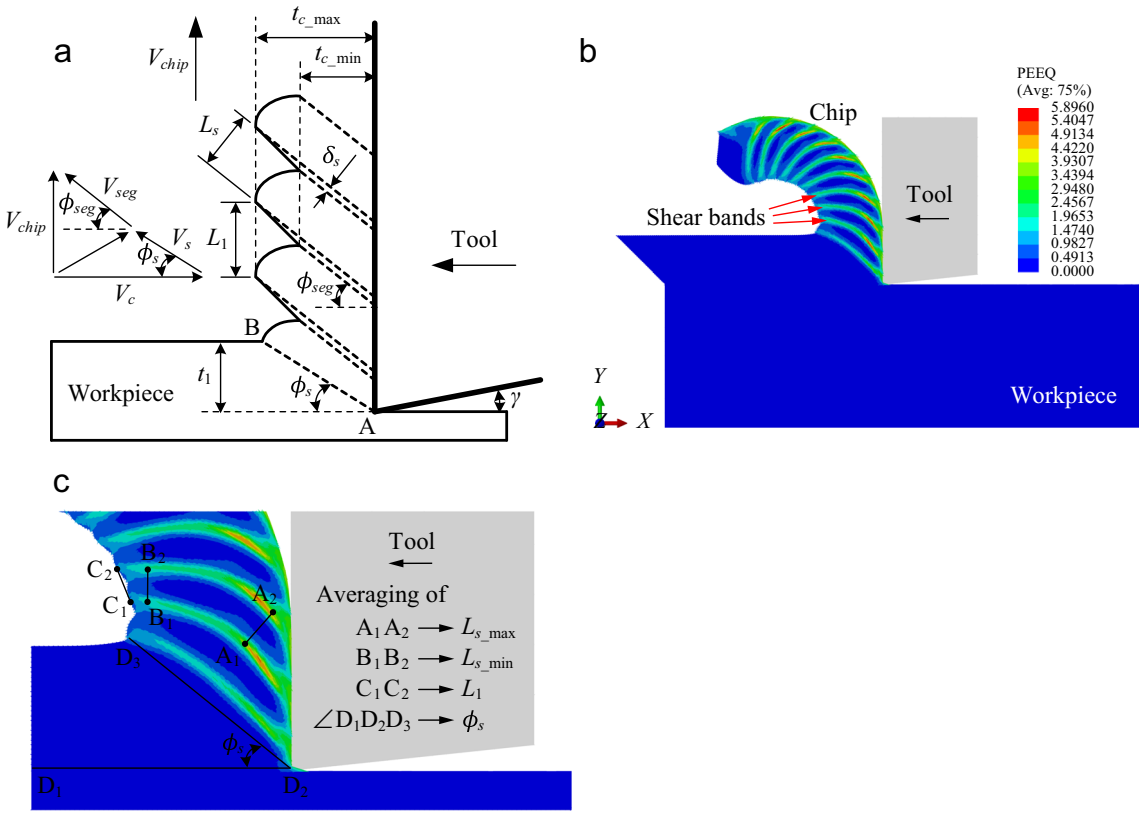

Fig. 2 **a** An idealized model for a regularly segmented chip with definitions of quantities and its hodograph. **b** A chip morphology obtained from FEM simulation of orthogonal cutting of Inconel 718 ($V_c = 40$ m/s, $t_1 = 200$ μm). **c** Characterizations of $L_{s\_max} = A_1A_2$, $L_{s\_min} = B_1B_2$, $L_1 = C_1C_2$ and $\phi_s = \angle D_1D_2D_3$ refer to Molinari et al. [33]

back surface. Therefore, L_s in Fig. 2c have to be viewed as the average value measured along the chip segment and it can be defined by

$$L_s = \frac{1}{2}\left(L_{s\_\max} + L_{s\_\min}\right) \tag{4}$$

The frequency of chip serration is the frequency of shearing plane formation determined from the chip geometry. Thus, the frequency of chip segmentation f_{seg} can be identified here with the number of segments produced per unit time [11, 41] as follows.

$$f_{seg} = \frac{N}{T_c} \tag{5}$$

where N is the number of segments, and T_c is the time of cutting.

In the serrated chip formation, each segment is limited by two shearing planes. Considering that the distance between neighboring teeth (known as the serrated chip pitch as shown in Fig. 2a) is equal to the chip segment length measured in the direction of tool rake face, the average velocity of chip V_{chip} sliding on the tool rake face can be estimated by

$$V_{chip} = f_{seg}\, L_1 \tag{6}$$

By applying the condition of the volume conservation that follows $V_c \cdot t_1 = V_{chip} \cdot t_{chip}$ in plastic deformation, the average thickness of chip t_{chip} sliding on the tool rake face with Eq. (6) is thus given by

$$t_{chip} = \frac{V_c \cdot t_1}{f_{seg} \cdot L_1} \tag{7}$$

From Fig. 2b and c, it can be found that the equivalent plastic strain (i.e., PEEQ) is mainly concentrated along the shear localized bands. But the shear bands are wider at the chip's back side than those at the chip's free side. The chip's serrated flow motion is quite inhomogenous since the workpiece materials inside shear bands are deformed seriously along the shear direction, while those outside the shear bands remain almost undeformed. The widely observed shear bands between sawteeth indicate that the serrated chip flow under high speed machining is closely related to the repeated shear banding.

3 Simulation results and discussion

3.1 Evolution of chip morphology

Chip morphologies with strain contours collected during the orthogonal cutting simulations at various speeds with the three used uncut chip thicknesses are shown in Fig. 3. It can be seen that at relatively low speeds within the high cutting speed range, the continuously smooth chips indicate homogeneous deformation without shear localized bands inside when the removed layer of material flows across the primary shear zone (chip formation region), whereas, at intermediately high cutting speeds, plastic deformation in the primary shear zone is not homogeneous and intense localized deformation is involved within the chip. Consequently, when shear bands penetrate the chip thoroughly, it is the serrated chip comprised of two distinct regions, i.e., the grossly inhomogeneous deformation with shear localization between neighboring segments and the relatively low deformation within individual segment bulks. With the advancing of cutting tool, the segment just formed seems to be crushed out of shape by the one being formed, thus, it is then pushed upwards on the tool rake face. But at extremely high cutting speeds, the disappearance of chip serration is observed. Shear bands even do not penetrate through the chip. The chips emerge as continuously smooth ones with shear localized bands inside.

At the relatively low cutting speed $V_c = 2$ m/s, the chips do not have shear bands, and they are continuously smooth similar to those encountered at conventional cutting speeds and feeds. For cutting speed $V_c = 6$ m/s, the onset of shear bands is observed. For cutting speeds $V_c = 40$ m/s and $V_c = 100$ m/s, the chips are regularly serrated in form and in frequency. The presence of all shear bands penetrating the chip thickness thoroughly is observed. For cutting speed $V_c = 150$ m/s, shear bands are more or less formed. Some shear bands even do not cross the entire chip thickness. For still higher cutting speeds $V_c = 200$ m/s and $V_c = 240$ m/s, the chips appear to be uniform in thickness. A family of shear bands is clearly seen within the chips accumulated at the chips' back side, but few of them can reach the free side of the chips. Many shear bands are activated and almost simultaneously growing within the chip formation region. Interaction between neighboring shear bands happens. A possible interpretation is that at this high level of cutting speeds, the shear bands do not have enough time to propagate from the tool tip to the chip's free surface. These shear bands are pushed away from the chip formation region by material convection due to chip flow before they can be fully developed. As shown in Fig. 3, the increasing cutting speed also seems to have the effect of reducing the average chip thickness. It must be noted that a certain irregularity of chip segmentation occurs at cutting speeds of high level. The measures presented in Fig. 2c are performed on chips with a total cutting length of 2 mm and more than 5 measurements for each quantity of each simulated chip. Therefore, the values of simulation results are symbolized by the corresponding average value.

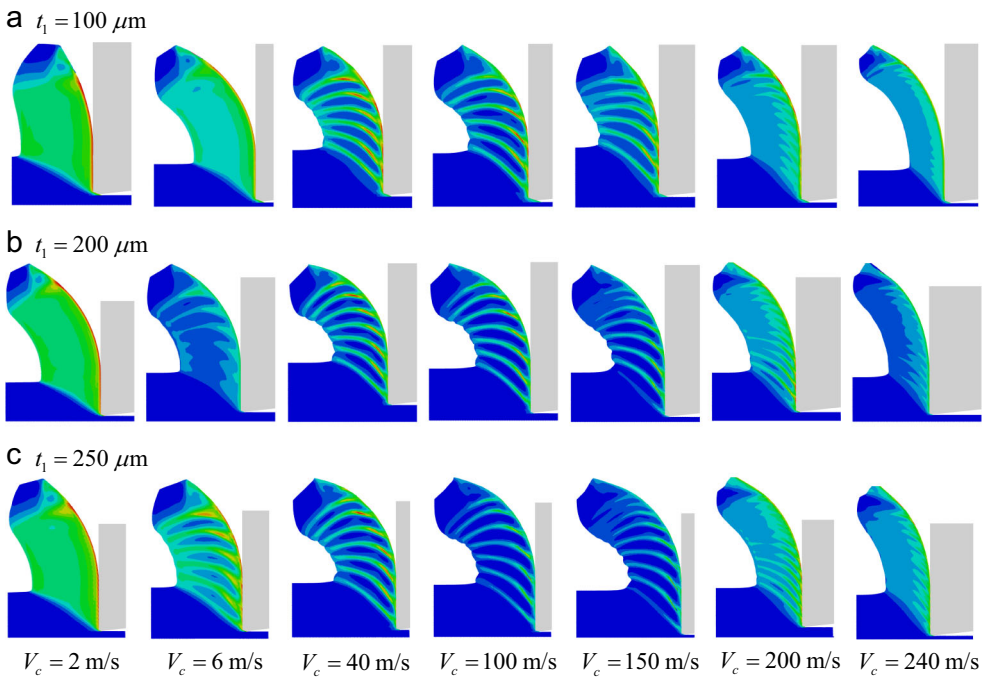

Fig. 3 Chip morphologies collected at various cutting speeds with three uncut chip thicknesses

3.2 Mechanism of serrated chip formation

Shear localized bands can develop during rapid deformation of high speed machining. Figure 4 shows a new shear band that propagates from the tool tip and through the entire chip thickness, and it clearly depicts the evolution of shear strain localization at a given cutting speed and a depth of cut. After a shear band is fully developed, the strain localization reaches a high level within the bands. Another new shear band will not nucleate at the tool tip before the one being formed is squeezed out of the primary shear zone. Therefore, interactions between neighboring shear bands will not arise within a regularly serrated chip.

Three main stages of the regularly serrated chip formation are summarized and schematically shown in Fig. 5 according to the evolution steps depicted in Fig. 4. In stage one, the workpiece material bulges with negligible deformation ahead of the advancing tool and a new shear band starts from the tool tip. During the second stage, the shear band runs almost parallel to the cutting velocity vector V_s as depicted in Fig. 2a, gradually propagates and concavely curves upwards until it meets the chip's free surface. In the third stage, the shear band propagates through the entire chip thickness. At this stage, highly intense concentrated shear band is formed, and it can be observed at the evolution steps of seven and eight, as shown in Fig. 4. It is interesting to note that the three main stages of the regularly serrated chip formation were also summarized based on the micrographs of collected chips by Wang et al. [42] in ultra-high speed machining of super alloy Inconel 718, and by Sutter and List [11] in the very high speed cutting of titanium alloy Ti-6Al-4V. Although nickel alloy Inconel 718 and titanium alloy Ti-6Al-4V are different, they share the common features. That is, they are both difficult-to-cut alloys and involve shear localization leading to the serrated chip formation. More specifically, they show similar changes of chip pattern with the cutting speed increasing.

Therefore, the creation of a new segment begins with the shear banding. Strain localization occurs in a narrow band in the primary shear zone leading to catastrophic shear failure along a shear plane, and this will result in the periodic formation of serrations at the chip's free surface. Crack can also be initiated and propagated from the tool tip to the chip's free surface during the regularly serrated chip formation.

3.3 Evolution of the shear angle

In the conventional cutting speed range, the shear angle ϕ_s is usually used as an efficiency parameter in machining. High value of ϕ_s corresponds to low strain in the chip and reduced energy consumption in the machining process [43]. The shear angle ϕ_s is the orientation of shear band in the primary shear zone (see Fig. 2c, defined by a line connecting the tool tip with a point at the serrated chip's free surface), and the segment inclination ϕ_{seg} shown in Fig. 2a results from ϕ_s amplified by a compression process where the workpiece material is pushed upwards on the tool rake face to form a new serration at the chip's free side. Therefore, the evolution of segment inclination ϕ_{seg} must be correlated with the evolution of shear angle ϕ_s. The study of shear angle ϕ_s and

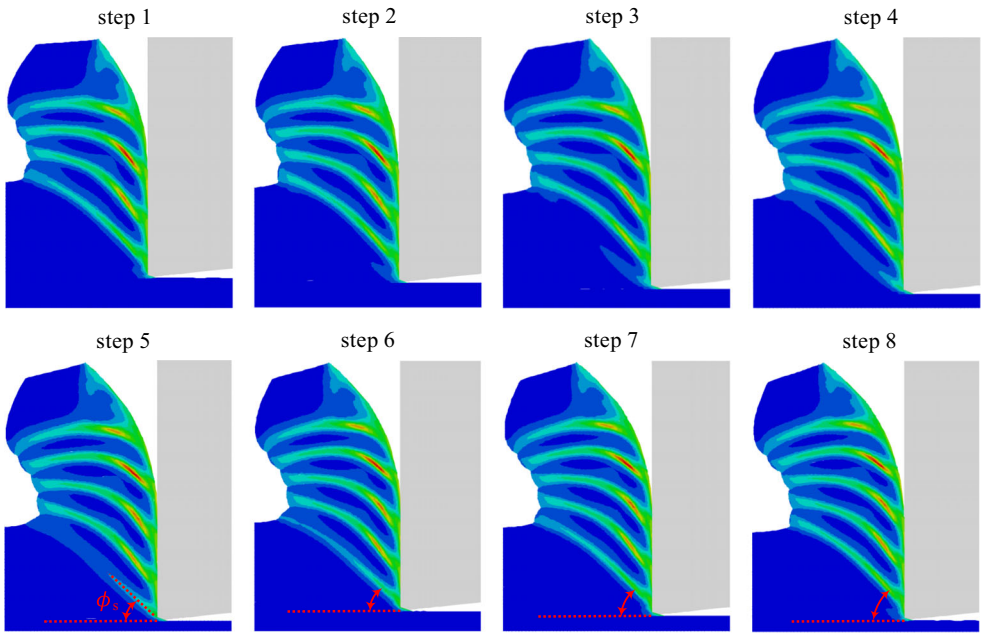

Fig. 4 Evolution steps of the regularly serrated chip formation simulated at cutting speed $V_c = 40$ m/s and uncut chip thickness $t_1 = 200$ µm

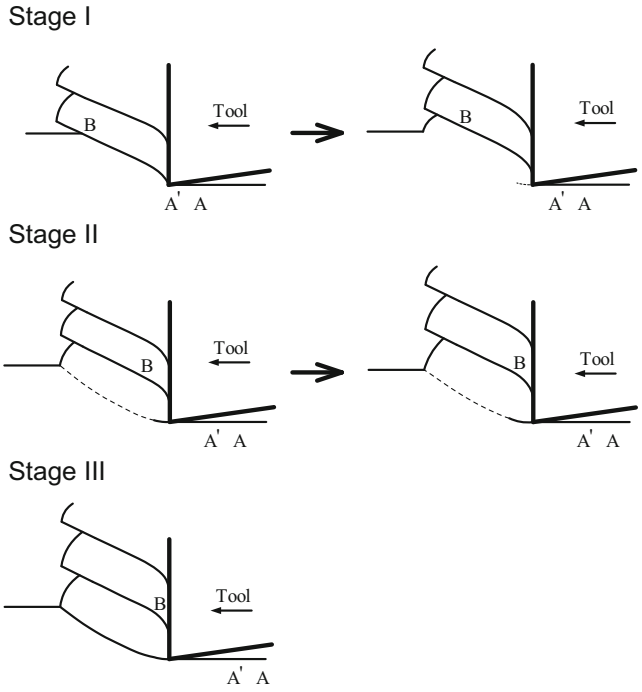

Fig. 5 Three main stages of the regularly serrated chip formation

segment inclination ϕ_{seg} can be useful for understanding the mechanism of chip formation of Inconel 718.

Figure 6a illustrates the evolutions of segment inclination ϕ_{seg} and shear angle ϕ_s against the cutting speed V_c, respectively. With V_c increasing, it can be seen that ϕ_{seg} decreases and tends to a limit value of 45°. The new shear angle ϕ_s is necessary lower than or finally equal to the segment inclination ϕ_{seg} to respect the principle of volume conservation. Indeed, ϕ_s increases from a small value and heads upwards to an asymptotic value of 45°, which corresponds to a minimum shear energy [11, 44] due to the fact that the increasing shear angle reduces the primary shear area [45]. It means that the shear angle ϕ_s increases with the cutting speed V_c but is always less than 45° with a zero-degree rake tool, and the segment inclination ϕ_{seg} is finally equal to the shear angle ϕ_s in the primary shear zone at very high cutting speeds. It is worth noting that the limit value of shear angle, i.e., 45°, is also expected in the continuous chip formation in high speed machining of other workpiece materials. For instance, the trend and its limit value were experimentally observed in the cases of a middle hard steel [22, 45], 6061-T6 aluminum alloy [43] and titanium alloy Ti-6Al-4V [11].

3.4 Evolution of shear band spacing

The shear band pattern in formation is governed by various conditions especially depending on the level of cutting speeds. Figure 7a shows the evolution of mean shear band spacing L_s in terms of cutting speed V_c for the three depths of cut t_1. It is found that L_s increases with t_1 and great changes of L_s happens as V_c increases. Figure 7b shows the evolution of normalized shear band spacing L_s/t_1 in terms of cutting speed V_c for the three depths of cut t_1. From Fig. 7a and b, it is seen that abrupt drops of shear band spacing happen and exist near to two cutting speeds, and they can be defined as the subcritical speed V_{crit}^- and the supercritical speed V_{crit}^+, respectively. Combining with Fig. 3, if the cutting speed is lower than the critical value V_{crit}^-, it is observed that the continuously smooth chip emerges with localized shearing inside the chip (not reaching the chip's free surface). If the cutting speed within the range $V_{crit}^- < V_c < V_{crit}^+$, the serrated chip with regular shear band spacing occurs, i.e., the shear bands are formed sequentially without interactions between neighboring ones. Although the chip is serrated, it depicts a macroscopically continuous form and the segments within the chip attach to each other, as shown in Fig. 4, which presents the evolution steps of a new shear localized band propagating through the entire chip thickness during the periodically serrated chip formation. But above the critical cutting speed V_{crit}^+, a totally different mechanism of shear band formation appears. At this high level of speeds, the tool advances so fast that a new shear band may be formed while the former one is still in action. Many shear bands do not penetrate through the entire chip thickness. A family of shear bands with irregular spacing and interactions between neighboring ones are both clearly observed within the chips in Fig. 3, and it is very different from the pattern of well developed shear bands separated by segments within the cutting speed range $V_{crit}^- < V_c < V_{crit}^+$.

It is worth noting that the almost monotonic decrease of shear band spacing with the cutting speed increasing in Fig. 7a and b is in accordance with the trend of experimental data for the high speed machining of titanium alloy Ti-6Al-4V by Molinari et al. [41] with cutting speed from 0.01 to 73 m/s based on a ballistic setup, and by Ye et al. [46] with cutting speed from 0.05 to 31.2 m/s based on the light-gas gun device. When the cutting speed is greater than a critical value, the shear band spacing has not much changed with the cutting speed increasing. This is in agreement with the simulation results by Molinari et al. [33] for titanium alloy Ti-6Al-4V with cutting speed up to 500 m/s, and also in agreement with the predicted results by Cai and Dai [47] based on the high speed machining experiments with cutting speed up to 15 m/s for titanium alloy Ti-6Al-4V and up to 10 m/s for Inconel 718.

It is also worth noting that in Fig. 7a, V_{crit}^- is sensitive to the depth of cut t_1, and it can be confirmed in Fig. 3 at $V_c = 6$ m/s by the emergence of shear localized bands within the chips for $t_1 = 200$ µm and $t_1 = 250$ µm but no shear localized bands arising within the chip for

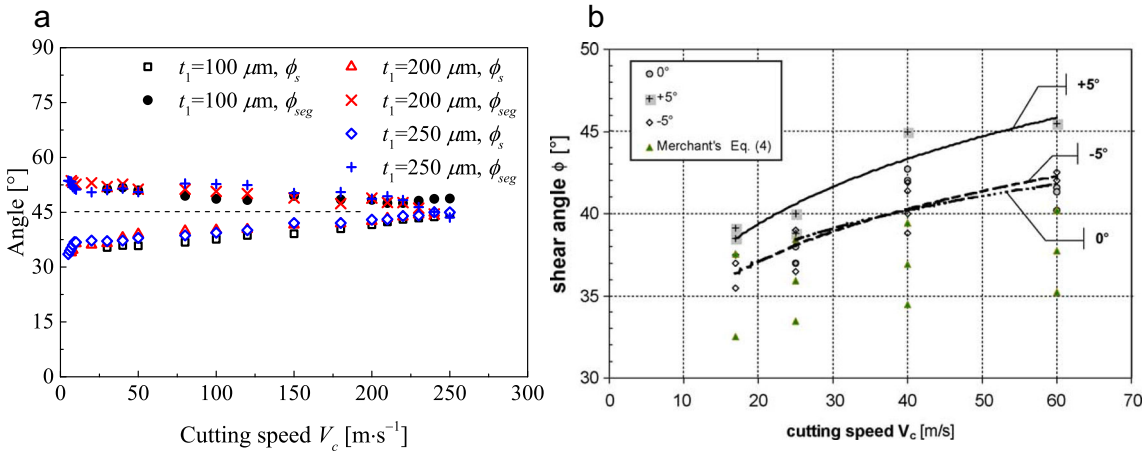

Fig. 6 **a** Segment inclination ϕ_{seg} and shear angle ϕ_s versus cutting speed V_c. **b** Evolution of shear angle ϕ versus cutting speed V_c with tool rake angle $\alpha = +5°, 0°, -5°$ and uncut chip thickness $t_1 = 0.25$ mm for a middle hard steel (French Standards XC18) [45]

$t_1 = 100$ µm. However, V_{crit}^{+} is almost insensitive to the depth of cut t_1 as can be observed in Fig. 7b at a fixed value. It also needs to point out that transition periods obviously exist when V_c is near to V_{crit}^{-} and V_{crit}^{+} to complete the transformation of chip types. The onset of chip serration (flow instability) happens for the cutting speed approaching V_{crit}^{-} and the disappearance of chip serration occurs after the cutting speed exceeding V_{crit}^{+}. Therefore, it is of great significance to qualify the values of V_{crit}^{-} and V_{crit}^{+} as precise as possible.

The normalized cutting speed is defined as $R_k = \frac{\rho C_p t_1 V_c}{k}$, as referred to Ref. [33]. Figure 8a shows the evolution of normalized shear band spacing L_s/t_1 in terms of normalized cutting speed R_k for the three depths of cut t_1. At low R_k, the data points tend to cluster together. A drop of L_s/t_1 is observed in Figs. 7b and 8a (more obvious corresponding to L_s at low V_c in Fig. 7a) and followed by a plateau. This phenomenon is adverse to the trend of simulation results, i.e., an increase of the shear band spacing followed by a plateau at low cutting speeds as shown in Fig. 8b, on cutting of titanium alloy Ti-6Al-4V with a fixed sliding friction coefficient ($\mu = 0.4$) performed by Molinari et al. [33]. This is because the friction between chip and tool rake face is neglected in this work. As R_k (or V_c in Fig. 7b) increases, another drop of L_s/t_1 but more abrupt happens and is followed by a lower plateau. More specifically, L_s drops dramatically to a small fraction of t_1 with an approximate value of 0.2 (also seen in Fig. 7b), which coincides with the simulation results on cutting of titanium alloy Ti-6Al-4V performed by Molinari et al. [33] at very high cutting speeds, as shown in Fig. 8b. At still higher speed $R_k > R_k^{+}$ (corresponding to $V_c > V_{crit}^{+}$ in Fig. 7b), it is seen from Fig. 3 at $V_c = 200$ m/s and $V_c = 240$ m/s that the shear bands interact with each other and shear band spacings are so small and irregular. This is very different from the shear band pattern with regular spacing and without interactions

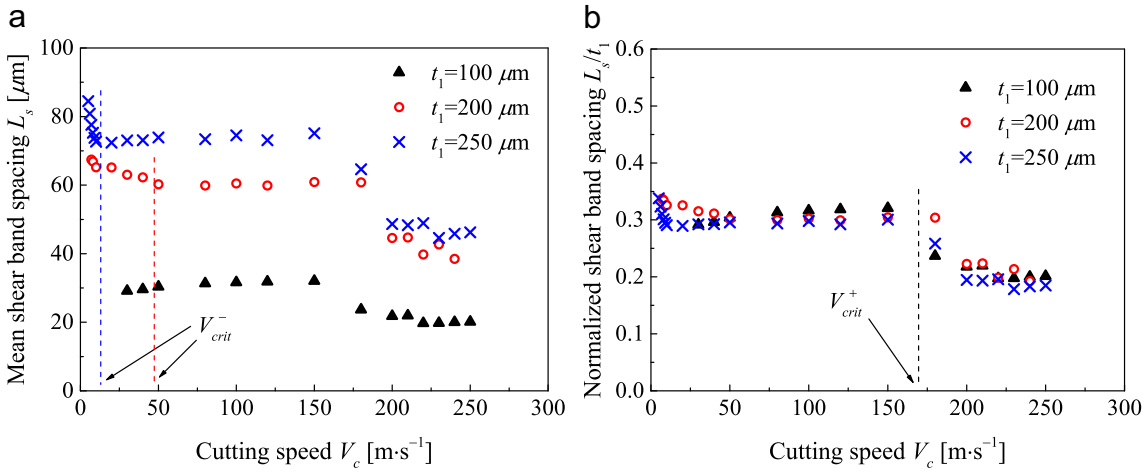

Fig. 7 **a** Mean shear band spacing L_s in terms of cutting speed V_c. **b** Normalized shear band spacing L_s/t_1 in terms of cutting speed V_c

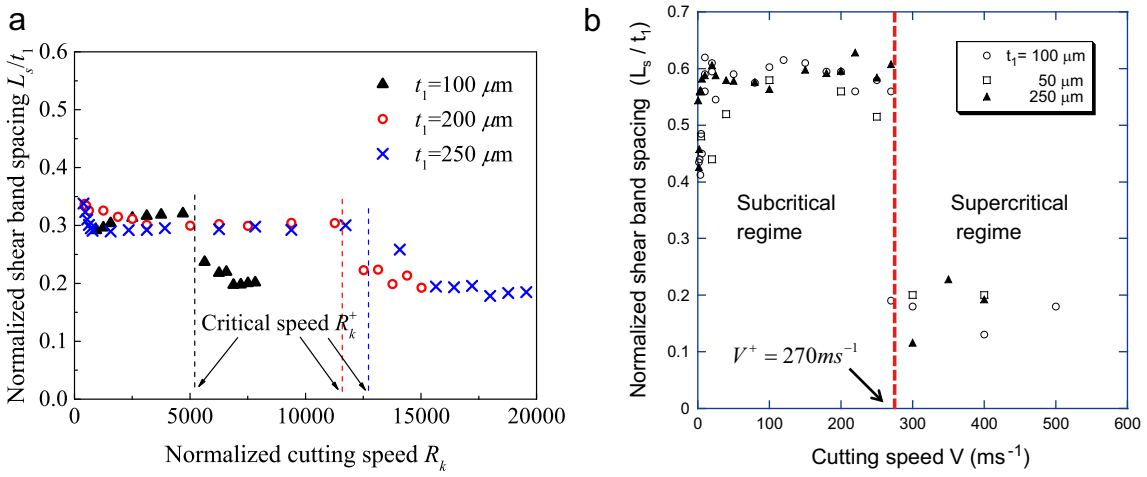

Fig. 8 **a** Normalized shear band spacing L_s/t_1 in terms of normalized cutting speed R_k. **b** Normalized shear band spacing L_s/t_1 in terms of cutting speed V in cutting simulations of titanium alloy Ti-6Al-4V with a fixed sliding friction coefficient $\mu = 0.4$ [33]

in Fig. 3 at $V_c = 40$ m/s and $V_c = 100$ m/s where $R_k < R_k^+$ (corresponding to $V_c < V_{crit}^+$ in Fig. 7b). From Figs. 7b and 8a, it is also seen that L_s/t_1 in the two successive plateau regions is almost independent of the cutting speed V_c (the normalized cutting speed R_k) and the depth of cut t_1. Moreover, L_s is proportional to the depth of cut t_1 in the plateau regions since L_s/t_1 almost remains at a fixed value respectively. But the value of R_k^+, at which L_s/t_1 suddenly drops, is obviously different from each other for the three t_1. In other words, the former plateau is less extended for a smaller t_1 in terms of R_k in Fig. 8a, but it has the same extension for the three t_1 in terms of V_c in Fig. 7b.

Note that R_k is inversely proportional to the low heat conductivity k of workpiece material. Adiabatic conditions are prevailing in shear bands when machining Inconel 718, and these are supported by many experiment and simulation results [2, 3, 14]. Besides, cutting speed influences the chip formation mechanism of Inconel 718, which involves shear localization in the shear zones [43, 48] since the heat generated by severe plastic deformation is unable to dissipate in time [41, 45]. Consequently, adiabatic conditions contribute to temperature rising and thus material softening in the shear zones, and it in turn influences the localized shear band formation especially when cutting speed crosses the critical value V_{crit}^- [49]. These thermal effects can be confirmed by the results mentioned above. That is, shear band spacing L_s (L_s/t_1) drops when cutting speed approaches V_{crit}^- and drops again to a lower plateau when cutting speed outstrips V_{crit}^+ (corresponding to R_k^+). But at high cutting speeds, inertia effects become significant. Furthermore, it has been demonstrated by Bonnet-Lebouvier et al. [50] that inertia effects can control shear band propagation through the chip formation region. Thus, it is concluded that inertia effects are involved for the decay of shear band spacing to a lower plateau when cutting speed $V_c > V_{crit}^+$. Finally, it can be deduced that thermal effects and inertia effects affect shear band spacing especially when cutting speed is near to V_{crit}^- and V_{crit}^+. However, their effects on shear band spacing are ineffective within the plateau regions with the cutting speed increasing.

Figure 9a displays mean shear band spacing L_s in terms of strain rate V_c/t_1 for the three depths of cut t_1. Figure 9b depicts mean shear band spacing L_s in terms of strain rate V_c/t_1 in a log-log diagram. It seems that the shear band spacing is a decrease function of the applied measure strain rate for cutting speed $V_c < V_{crit}^-$ or $V_c > V_{crit}^+$. It is noticed that this feature has been confirmed by experimental results and theoretical analyses in Refs. [51, 52]. In addition, two successively significant drops of L_s are seen in Fig. 9a and b as cutting speed increases before reaching V_{crit}^- and after exceeding V_{crit}^+. For cutting speed $V_c < V_{crit}^+$, the two distinguished regions of shear band spacing L_s and the evolutions of L_s in terms of V_c/t_1 in a log-log diagram are displayed in Fig. 10a for the three depths of cut t_1. The results show that a slight fall of L_s happens when cutting speed is lower than the critical value V_{crit}^-, as seen in Figs. 9b and 10a. The values of L_s are then constants for the three depths of cut t_1 when cutting speed exceeds V_{crit}^- but less than V_{crit}^+. However, when cutting speed passes V_{crit}^+, the mean shear band spacing L_s in terms of the strain rate V_c/t_1 in a log-log diagram displayed in Fig. 10b sees a different pattern, that is, L_s linearly decreases with a slope of -0.94 as V_c/t_1 increases in a log-log diagram.

3.5 Evolutions of cutting force and chip segmentation

The emergence of periodically serrated chip is found to be related to the thermoplastic shear instability occurring in the shear zones [53, 54], and it is often referred to the formation

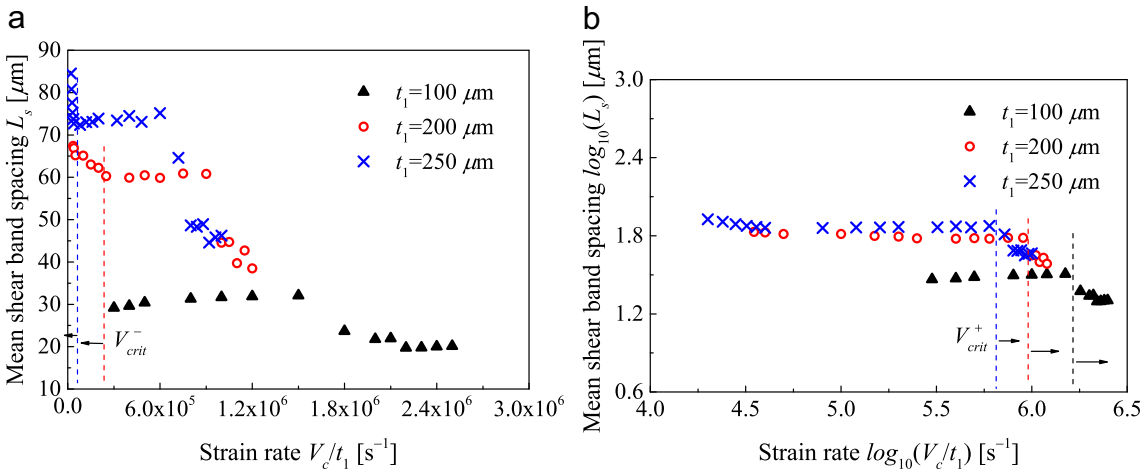

Fig. 9 **a** Mean shear band spacing L_s in terms of strain rate V_c/t_1. **b** Mean shear band spacing L_s in terms of strain rate V_c/t_1 in a log-log diagram

of adiabatic shear bands [51]. This mechanism of chip formation is quite different from that encountered at conventional speeds and feeds because the plastic instability is more intense and is accompanied with amplified phenomena of ductile or brittle fracture. Due to the high speed, the dynamics of cutting itself have changed, particularly with regard to the chip removing. The evolution of cutting force F_c plotted against cutting time T_c is described in Fig. 11a with the cutting speed $V_c = 30$ m/s and the uncut chip thickness $t_1 = 250$ µm. It is also noticed that the calculation measure of average cutting force F_{ave} is depicted in Fig. 11a. It must be pointed out that for the continuously smooth chip flow, the cutting force is almost constant after the cutting process is stabilized. But for the periodically serrated chip flow, a cyclic variation of cutting force is produced, as shown in Fig. 11a.

The fluctuation of cutting force shown in Fig. 11a can be explained by the phenomenon of chip serration in the cutting process. As can be seen, the cutting force stabilizes after the second cycle. Combined with the evolution steps of the regularly serrated chip formation in Fig. 4, it is easy to find that the stabilized cyclic of the cutting force begins just after a serration initiates from the step two. At this point, the region around the tool tip is at elevated temperatures (see Fig. 11b), and thus softer than the surrounding materials. As the tool advances, the shear localized zone widens and slides upwards (see step three to five in Fig. 4) on the tool rake face. However, the upward movement of the shear localized zone causes the tool to plough through stronger materials that leads to a rise of the cutting force. Then, the cutting force is reduced due to the growth of the shear localized zone that leads to the increase of shear angle (see ϕ_s from step five to eight as depicted in Fig. 4), which is associated with the decrease of the primary shear plane area and thus the consumed shear energy. Therefore, as long as another serration is formed, the serrated chip formation

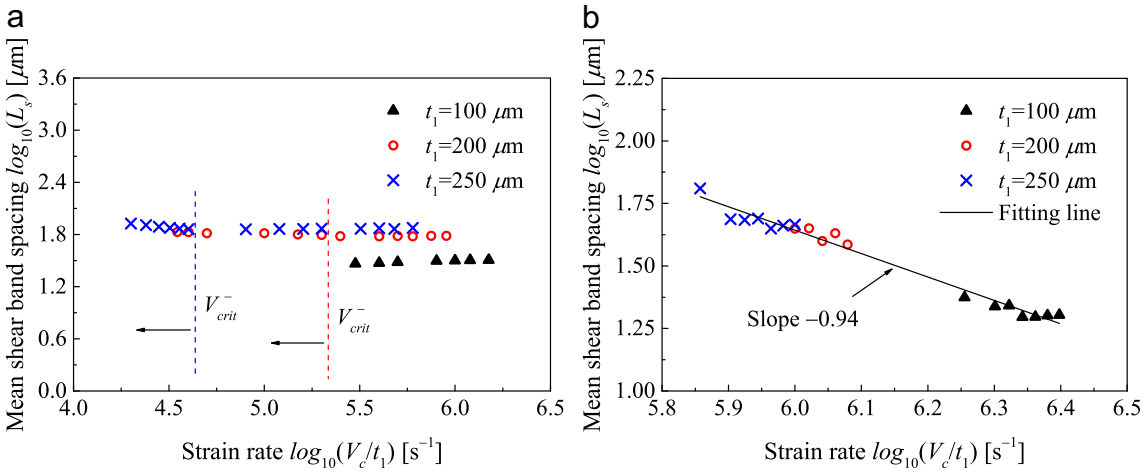

Fig. 10 **a** Mean shear band spacing L_s in terms of strain rate V_c/t_1 in a log-log diagram when $V_c < V_{crit}^+$. **b** Mean shear band spacing L_s in terms of strain rate V_c/t_1 in a log-log diagram when $V_c > V_{crit}^+$

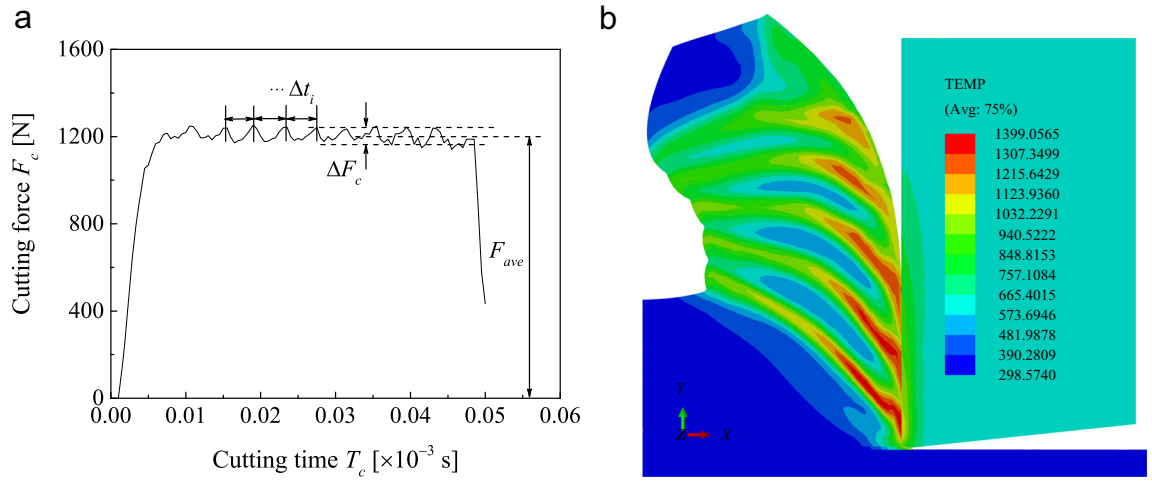

Fig. 11 Simulation results with the cutting speed $V_c = 30$ m/s and the uncut chip thickness $t_1 = 250$ µm. **a** Cutting force F_c versus cutting time T_c. **b** Temperature distribution

process follows a repetitive pattern. The cycles of the cutting force correspond to the formation of the shear localized zones, and this has also been explained in Ref. [55] by the fluctuation of cutting force for ductile iron during the serrated chip formation.

Thus, the cutting force frequency f_{force} can be calculated by the average value of $\frac{1}{\Delta t_i}$ $(i = 1, 2, 3, \cdots)$. The time interval Δt_i is the oscillation period of cutting force between two successive peaks as depicted in Fig. 11a. The frequency of chip segmentation f_{seg} is derived from the chip morphologies by utilizing Eq. (5). The results presented in Fig. 12a show that f_{force} and f_{seg} keep steps closely with each other as they evolve. Combined with the evolution steps of a new shear band propagation depicted in Fig. 4, it is noted that the serrated chip's free side looks like a tooth once a shear localized band penetrates the chip thoroughly and each tooth corresponds to a segment. Therefore, it is concluded that the time interval Δt_i corresponds to the formation of successive shearing bands, and the frequency of cutting force oscillation f_{force} is closely associated with the frequency of chip segmentation f_{seg}. Furthermore, both kinds of the frequency linearly increase with the cutting speed when $V_c < V_{crit}^+$ for the three depths of cut t_1. This agrees with the direct proportion relationship $f_{seg} = \frac{t_1}{t_{chip} \cdot L_1} \cdot V_c$ derived from Eq. (7). However, intense increases for the two kinds of frequency are seen when cutting speed $V_c > V_{crit}^+$. It is worth noting that the segmentation frequency clearly increases with the cutting speed and decreases with the increase in feed are also shown in Fig. 12b for titanium alloy Ti-6Al-4V in Ref. [56] with cutting speed from 4 m/min to 140 m/min on a specially adapted lathe, and also for titanium alloy Ti-6Al-4V in Ref. [11] with cutting speed from 5 m/s to 75 m/s based on a specific ballistic setup, and for aluminum 7075 (1000–3500

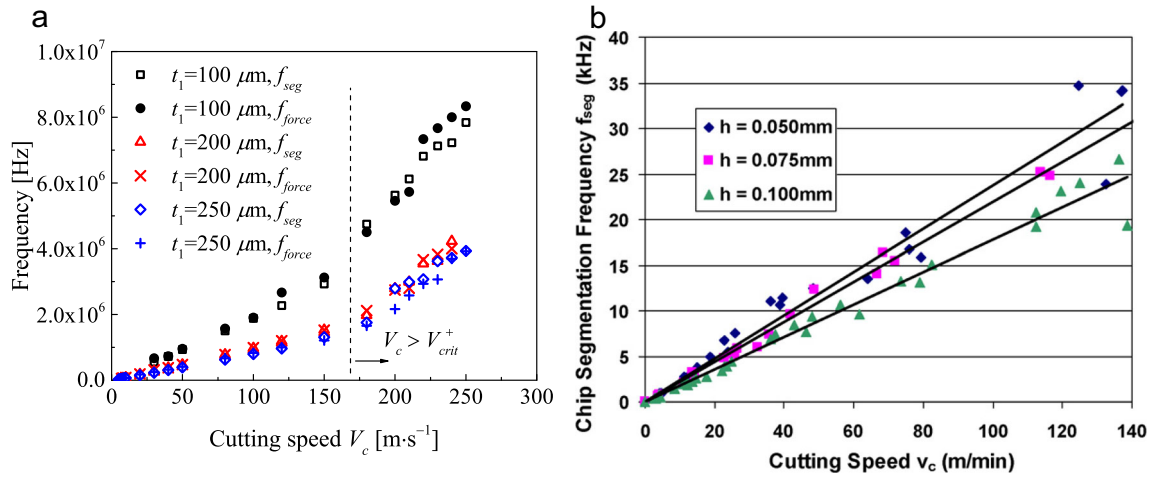

Fig. 12 **a** Cutting force frequency f_{force} and chip segmentation frequency f_{seg} versus cutting speed V_c. **b** Chip segmentation frequency f_{seg} versus cutting speed V_c during orthogonal cutting of titanium alloy Ti-6Al-4V [56]

m/min), harden steel 1045 (300–1500 m/min) and titanium alloy Ti-6Al-4V (100-1500 m/min) in Ref. [57] during high speed machining experiments.

In the overall range of cutting speeds, the results presented in Fig. 13a show that there is a clearly linear relationship between the chip segmentation frequency f_{seg} and the cutting speed V_c, i.e., a slope of 1.3 in a log-log diagram. This agrees well with the linear trend (slope = 1.4) of experiment results of the chip segmentation frequency as a function of the cutting speed in a log-log diagram in the high speed machining of titanium alloy Ti-6Al-4V obtained by Molinari et al. [41], as shown in Fig. 13b. Besides nickel alloy Inconel 718 and titanium alloy Ti-6Al-4V, it is interesting to find that the frequency of periodically serrated chip flow showing a power-law scaling with the cutting speed was also observed for AISI 4340 steel and aluminum 7075 (slope = 1.25) by Ye et al. [58] performing the high speed cutting experiments by using a light-gas gun device.

At this point, the simulation tendency in this work compares well with the published experimental measurements although the workpiece materials are distinct. The common feature is that these metals or alloys all involve shear localization leading to the serrated chip formation and thus show similar changes of chip pattern with the cutting speed increasing. Besides, it can be noted in Fig. 13a that the slopes are identical for the three depths of cut t_1. This means that these slopes do not depend on the depth of cut. It also shows in Fig. 13a that the chip segmentation frequency f_{seg} decreases with the increase in depth of cut t_1, and this dependence is observed for the cutting force frequency f_{force} with the depth of cut t_1 in Fig. 12a as well.

The dependence of average cutting force F_{ave} with respect to cutting speed V_c is described in Fig. 14a under the three depths of cut t_1. On the evolution, a slight fall of F_{ave} is observed at relatively low speeds within the high cutting speed range. Meanwhile, combining with Fig. 6a, it is easy to recognize that the shear angle ϕ_s increases in cutting as the speed progresses. This indirectly implies that the cutting force decreases while the shear angle increases. It should be remembered that adiabatic conditions contribute to temperature rising and material softening in the shear zones, and this is beneficial to shear banding especially when cutting speed crosses the critical value V_{crit}^{-} (the onset of the serrated chip). Therefore, when referring to the cutting speed ranging from 6 m/s to 40 m/s as shown in Fig. 3, it is found that the chips show a trend of strong shear localization. Shear bands within the chips submit to extrusion and are increasingly deformed. Thus, adiabatic shear banding during chip formation explains why the cutting force has a slight reduction. But F_{ave} increases with cutting speed continuously progressing in Fig. 14a, almost linearly increasing particularly when cutting speed $V_c > V_{crit}^{+}$. This trend is related to the resistance from chip flow since the materials do not have enough time to be evacuated due to the fact that the inertia effects are significantly involved at high cutting speeds where the thermal effects do not have predominance. As can be seen, these observations are more clearly displayed for specific cutting force F_{ave}/t_1 versus cutting speed V_c as shown in Fig. 14b. For the cutting speed range from 0 m/s to 120 m/s, the scattered points of specific cutting force in Fig. 14b tend to be a concave shape, and it agrees with the trend of experimental data in the machining of titanium alloy Ti-6Al-4V [11, 41, 59, 60]. The demarcation lines (at which the specific cutting forces are minimum) in Fig. 14b, where the inertia effects start to become significant, are also marked out for the three depths of cut t_1. That is, the inertia effects

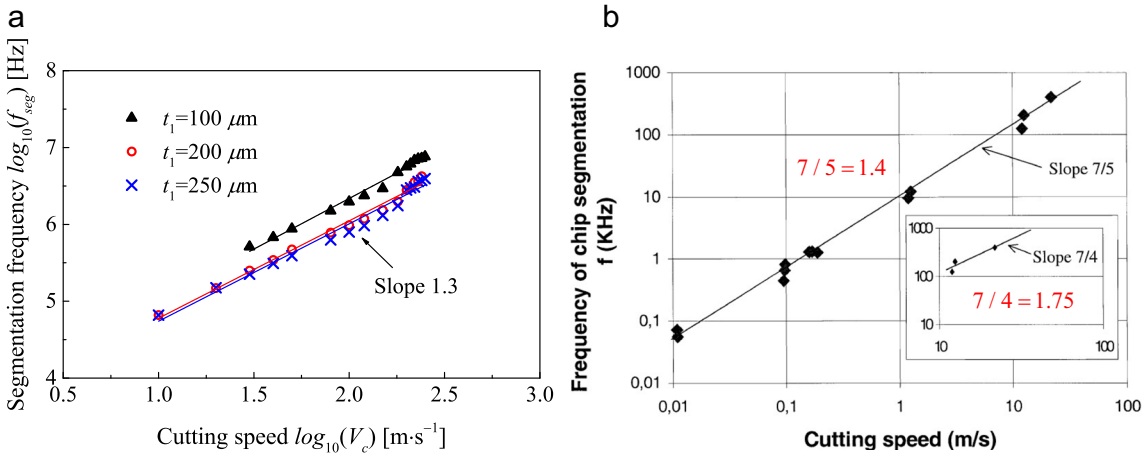

Fig. 13 **a** Chip segmentation frequency f_{seg} in terms of cutting speed V_c in a log-log diagram in the overall range of cutting speeds. **b** Frequency of chip segmentation f as a function of cutting speed V in a log-log diagram with tool rake angle $\alpha = 0°$ in high speed machining of titanium alloy Ti-6Al-4V [41]

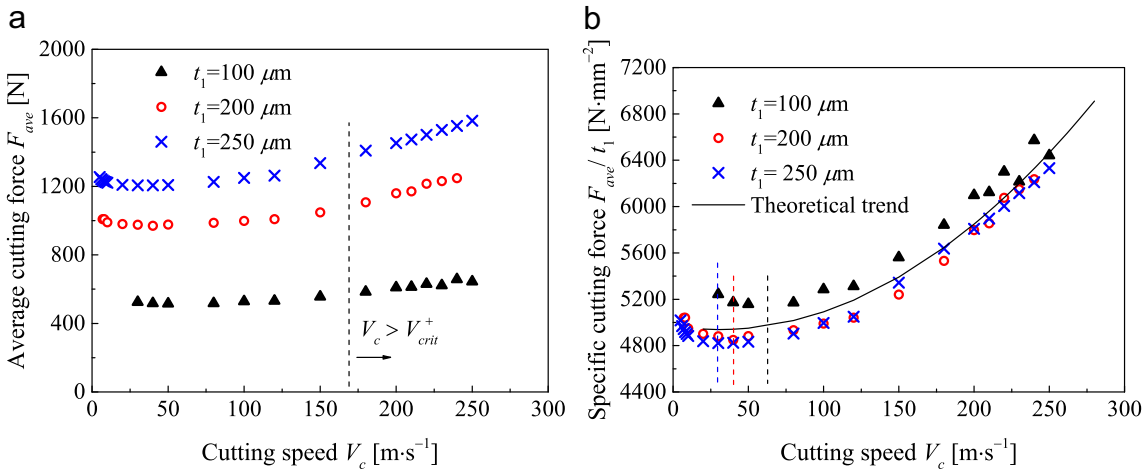

Fig. 14 **a** Average cutting force F_{ave} versus cutting speed V_c. **b** Specific cutting force F_{ave}/t_1 versus cutting speed V_c

produce an increase of the cutting force beyond a certain characteristic cutting speed, as is also concluded in Ref. [61] for CRS 1018 steel.

Just like the resultant force F_R plotted in Fig. 15 in metal cutting, it is a fundamental that the cutting force F_c from the orthogonal cutting simulation displayed in Fig. 11a can also be resolved into quasistatic and dynamic solutions as follows.

$$F_c = F_{static} + F_{dynamic} \tag{8}$$

According to the studies of Dudzinski and Molinari [61], Recht [62] and Arndt [63], all forces created by interaction of the tool and the chip as shown in Fig. 15 are due to the shearing force F_s (in combination with the shear angle ϕ_s) and the inertia force F_m (the momentum change from the workpiece state to the chip state). The force per unit width of cut has been considered since the 2D-FEM model for orthogonal cutting simulations is adopted in Fig. 1b. Thus, the inertia force F_m is given by [61–63]

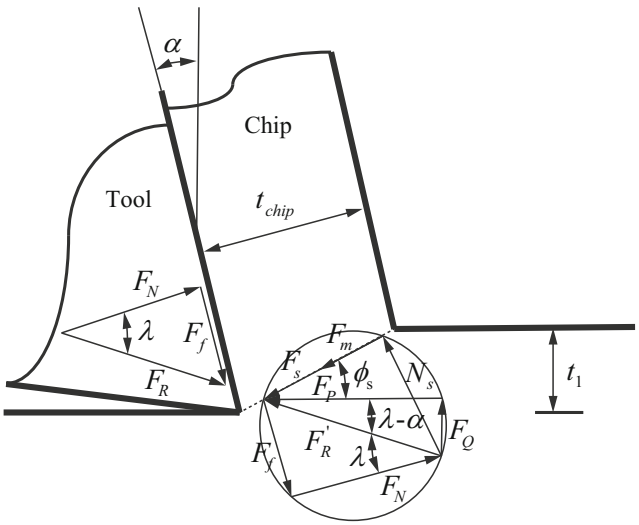

Fig. 15 Forces at the tool-chip interface and at the output of the shear zone [61]

$$F_m = \frac{t_1 \rho V_c^2 \cdot \cos(\alpha)}{\cos(\phi_s - \alpha)} \tag{9}$$

In this work, the tool rake angle $\alpha = 0°$. At high cutting speeds, the overall friction coefficient is small [34] (friction angle $\lambda \approx 0°$) and the shear angle ϕ_s is close to 45°, as mentioned above. The momentum loss caused by the state change in flow direction from the uncut workpiece material to the chip becomes very considerable, and it is independent of any particular cutting mechanism. The quantity of the so-called momentum force F_m is a purely dynamic effect [63], and it is parallel to the shear velocity vector [62, 63] as V_s in Fig. 2a. Therefore, combining with Eqs. (8) and (9), the specific cutting force is estimated by

$$\frac{F_{ave}}{t_1} = \frac{(F_s + F_m) \cdot \cos(\lambda - \alpha)}{t_1 \cdot \cos(\phi_s + \lambda - \alpha)} \approx \frac{\sqrt{2} \cdot F_s}{t_1} + 2 \cdot \rho V_c^2 \tag{10}$$

It should be remembered that at conventional cutting speeds, the inertia force F_m may be neglected compared to the shearing force F_s [62]. With the cutting speed increasing, the inertia force F_m plays a significant role since the momentum change from the workpiece state to the chip state becomes important, while the material strength, provided the "fluid state" has been reached, eventually loses its effect completely [63]. But at intermediate stage, the shearing force F_s and the inertia force F_m must both be considered.

Therefore, for relatively low speeds within the high cutting speed range, it is considered that $\frac{F_{ave}}{t_1} \approx \frac{F_s \cdot \cos(\lambda-\alpha)}{t_1 \cdot \cos(\phi_s+\lambda-\alpha)}$. At intermediately high cutting speeds, the theoretical trend with Eq. (10) shown in Fig. 14b must has a minimum value. At extremely high cutting speeds, Fig. 14b shows that the theoretical trend (i.e., $\frac{F_{ave}}{t_1} \propto (V_c)^2$) with Eq. (10) fits well with the trend of simulation results (i.e., parabolic growth),

and this was also observed with the FEM data in cutting simulations of titanium alloy Ti-6Al-4V by Molinari et al. [33]. It is worth noting that the feature of the cutting force decreasing with the cutting speed to a minimum at a characteristic speed has been confirmed by Flom et al. [43] for AISI 4340 steel and 6061-T6 aluminum alloy. Furthermore, beyond that characteristic speed, they also confirmed that the cutting force tends to slowly increase because the momentum force becomes significant at very high cutting speeds. The existence of the minimum cutting force was also reported in Ref. [64] for steel AISI 1045 during the orthogonal cutting experiments with the cutting speed up to 6000 m/min. Apart from these, it is also shown in Ref. [65] for titanium alloy Ti-6Al-4V by the simulations that the experimentally observed decrease of the cutting force with the cutting speed increasing and then the plateau at high cutting speeds less than 100 m/s are reproduced, and in Ref. [66] that the cutting forces are decreasing in the continuous and the segmented chip formation with the cutting speed up to 8000 m/min for aluminum alloy 7075 in milling experiments. Besides, Fig. 14b also depicts that the minimum value of F_{ave}/t_1 depends on the depth of cut t_1 (5156.99 N mm^{-2} for $t_1 = 100$ µm, 4848.45 N mm^{-2} for $t_1 = 200$ µm, 4822.00 N mm^{-2} for $t_1 = 250$ µm), and it agrees with the relationship that F_{ave}/t_1 is inversely proportional to t_1 in Eq. (10), i.e., $\frac{F_{ave}}{t_1} \propto (t_1)^{-1}$. Finally, for practice application, these relationships mentioned above need to be calibrated precisely from a data modeling.

3.6 Evolution of segmentation degree

The parameter of segmentation degree D_s is often used to quantify the intensity of chip serration for difficult-to-cut metals like hardened steels [67], titanium alloys [11] and nickel-based superalloys [40] at the industrially used cutting speeds and feeds. It varies between 0 and 1. In the case of $D_s = 0$, a continuously smooth chip, i.e., the uniform chip with no serration or with localized shearing inside, is produced. If $D_s = 1$, a completely broken chip is generated. Combined with Eqs. (2) and (7), it is given that $D_s = \frac{2\cdot(t_{c\_\max} - t_{chip})}{t_{c\_\max}}$.

The evolution of segmentation degree D_s in terms of cutting speed V_c is reported in Fig. 16a for the three depths of cut t_1. As can be seen, D_s shows a dependency on the cutting speed V_c and the depth of cut t_1. For a restricted range of cutting speed V_c less than 50 m/s, the segmentation degree D_s has a positive correlation with the cutting speed V_c. Similarly, the rise of segmentation degree is also pictured in Ref. [68] before the speed of 200 m/min for high strength alloy steel AerMet100 during the orthogonal cutting experiments, and in Ref. [69] for titanium alloy Ti-6Al-4V by the simulations and by the high speed milling experiments with the cutting speed up to 2500 m/min, and in Ref. [66] for aluminum alloy 7075 with the milling experiments by increasing the cutting speed up to 7000 m/min. Then the segmentation degree D_s in Fig. 16a is followed by a saturation before decreasing significantly at still higher cutting speeds (above 175 m/s). Combined with the chip morphologies collected in Fig. 3, it is concluded that D_s increases with the intensity of shear localized strain, which is the ratio of the average strain in a shear localized band by the average strain in a neighboring segment [25]. Therefore, higher intensity of shear localized strain means higher degree of chip segmentation in the machining of Inconel 718. It is worth noting that the scattered points of chip segmentation degree in Fig. 16a tends to be a convex

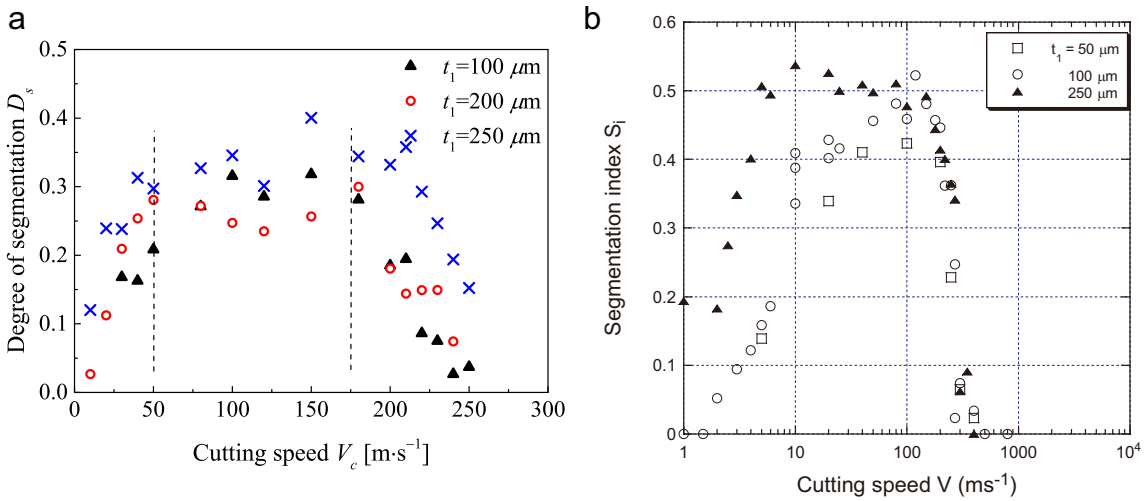

Fig. 16 **a** Segmentation degree D_s in terms of cutting speed V_c. **b** Segmentation index S_i versus cutting speed V in cutting simulations of titanium alloy Ti-6Al-4V with a fixed sliding friction coefficient $\mu = 0.4$ [33]

shape, which agrees with the trend of FEM data from the orthogonal cutting simulations of titanium alloy Ti-6Al-4V by Molinari et al. [33], as shown in Fig. 16b.

Referring to Fig. 14b, it is seen that specific cutting force F_{ave}/t_1 in terms of cutting speed V_c evolves in the opposite trend when compared to the evolution of D_s, as shown in Fig. 16a. This makes sense since a higher value of D_s is associated with a higher intensity of shear strain localization and then a higher temperature within shear bands that can induce a decrease of cutting force by thermal softening of materials in the shear zones. It is noticeable in Fig. 16a that D_s rapidly grows for the defined cutting speeds less than 50 m/s and sharply drops from the cutting speed about 175 m/s. In view of the overall situation, for the relatively low cutting speeds, it is recalled that the process of shear banding is mainly controlled by the thermal effects. Increasing the cutting speed promotes the adiabatic conditions and the arising of the serrated chips, and it in turn contributes to thermal softening and flow instability. As a result, it leads to the higher strain concentration within shear bands and the increase of D_s. For still higher cutting speeds, inertia effects are significant and in dominance as mentioned above. It hinders the movement of materials subject to high accelerations within the shear zones, thus contributing to the decrease of D_s by slowing down plastic flow localization, i.e., the process of shear strain concentration.

3.7 Evolutions of chip thickness and velocity

The dependence of average chip thickness t_{chip} with respect to cutting speed V_c is shown in Fig. 17a for the three depths of cut t_1. As can be seen, the increasing cutting speed V_c has the effect of reducing the average chip thickness t_{chip}. It can be noted in Ref. [70] that this effect has also been observed in high speed turning of Inconel 718. Just similar to the plateaus of shear band spacing shown in Figs. 7b and 8a, there also finally exists a plateau as the average chip thickness t_{chip} evolves where t_{chip} is almost independent of the cutting speed V_c and is equal to the corresponding depth of cut t_1.

The chip thickness ratio r_c is also used as an efficiency parameter in machining. Generally, the higher the value of r_c, the more efficient the cutting process [71]. By defining the chip thickness ratio $r_c = \frac{t_1}{t_{chip}}$, the evolution of r_c in terms of cutting speed V_c is shown in Fig. 17b. As can be seen, r_c increases and finally approaches an asymptotic value of one, which means that the average chip thickness t_{chip} is finally equal to the uncut chip thickness t_1 at very high cutting speeds. It also implies that the chip is thicker than the uncut chip when r_c is less than one. This is due to the fact that the gradual bulging of chip segment pushes the previously formed chip segment upwards during the serrated chip formation, as shown in Fig. 4. Then, the extrusion between segments delays the plastic deformation flow at the tool-chip interface, and soon afterwards the chip widens in thickness during the upward movement on the tool rake face by an upsetting process of segments. It is worth noting that the increasing trend of chip thickness ratio in terms of cutting speed and its asymptotic value of one has also been observed for 6061-T6 aluminum alloy in Ref. [43] and for a middle hard steel (French Standards XC18) in Ref. [45]. At this point, combined with Fig. 6a, it is seen that ϕ_s is close to 45° when $r_c = 1.0$. This coincides with the relationship of shear angle ϕ_s and chip thickness ratio r_c in Refs. [43, 71] where $\phi_s = \tan^{-1}\left(\frac{r_c \cos\alpha}{1 - r_c \sin\alpha}\right)$.

The average velocity of chip V_{chip} sliding on the tool rake face in terms of the cutting speed V_c is displayed in Fig. 18 for the three depths of cut t_1. It is observed that V_{chip} is almost linearly proportional to V_c with a slope very

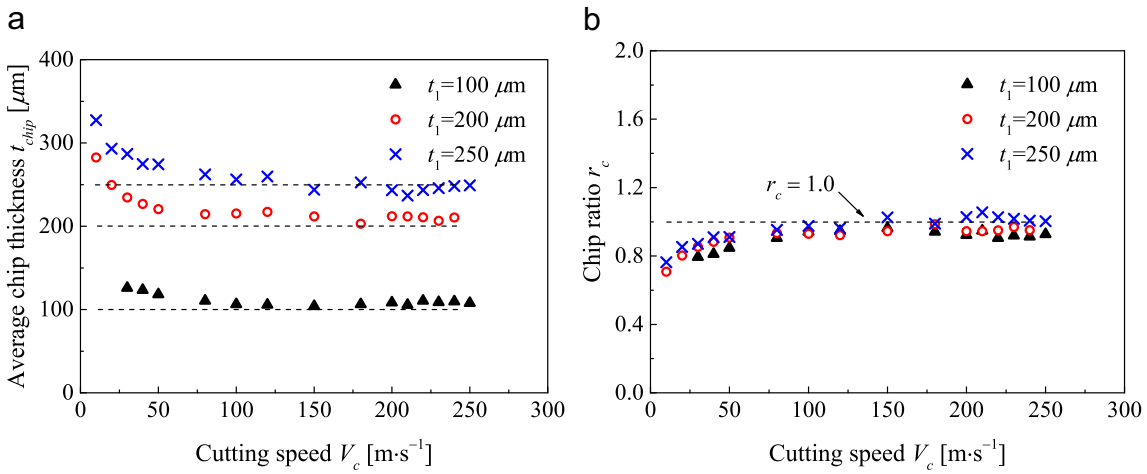

Fig. 17 **a** Average chip thickness t_{chip} with respect to cutting speed V_c. **b** Chip thickness ratio r_c in terms of cutting speed V_c

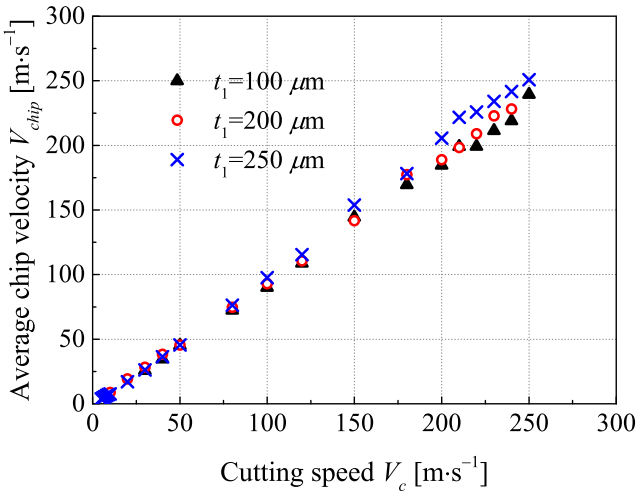

Fig. 18 Average chip velocity V_{chip} in terms of cutting speed V_c

close to 1.0, which indicates that V_{chip} is almost equal to V_c, i.e., the "fluid state" of cutting has almost been achieved. Although the results are a little bit dispersed at very high cutting speeds above 175 m/s, it can be attributed to some measurement errors or simulation factors.

3.8 Experiment validation of the model

In order to validate the developed FEM model, high speed cutting experiments of Inconel 718 based on the vertical CNC milling machine (GX710PLUS) are carried out. The four-fluted carbide end mill (AlCrN coating) with the rake angle $\alpha = 10°$ is used. The radial depth of cut $a_e = 0.1$ mm and the axial depth of cut $a_p = 2$ mm. The helix angle can then be considered to be zero in the end milling, as is studied by Altintas [72]. The cutting of each micro edge on the end mill can be regarded as a shaving process. Thus, the varied uncut chip thickness t in Fig. 19a is symbolized by its average value t_{ave}, which can be considered as the depth of cut t_1 in Fig. 1a, and t_{ave} is calculated from the swept zone as [72]

$$t_{ave} = \frac{\int_{\phi_{st}}^{\phi_{ex}} f_z \sin\phi d\phi}{\phi_{ex} - \phi_{st}} = -f_z \frac{\cos\phi_{ex} - \cos\phi_{st}}{\phi_{ex} - \phi_{st}} \tag{11}$$

where f_z is the feed rate (mm/rev-tooth) and ϕ is the instantaneous angle of immersion. ϕ_{st} and ϕ_{ex} are the cutter entry and exit angles, respectively.

For the FEM model in simulations, the mesh inclination angle δ at zone A is still kept the same as 45° with the tool rake face, as is set in Fig. 1b. As mentioned in the introduction, cutting speed from 50 m/min (0.83 m/s) can be considered as high speed milling of nickel alloys. Thus, in consideration of the end mill's strength and abrasiveness, the cutting speeds V_c are then selected as 50 m/min, 80 m/min and 110 m/min, respectively. The pictures of chip morphologies from experiments are captured by the optical microscope (Olympus dsx100) after milling. As shown in Fig. 19b, c and d, the simulated chip morphologies and their features agree well with the corresponding experimental observations, respectively. This indicates that the developed FEM model can produce good predictions for the chip deformation characteristics of the nickel-based superalloy Inconel 718.

4 Conclusions

Chip morphologies in the orthogonal cutting simulations of Inconel 718 are investigated at various cutting speeds with three depths of cut. The originality of this work lies in the relatively wide range of cutting speeds explored in the simulations. The JC constitutive law with the criterion of the accumulated plastic strain is adopted to model the plastic deformation of Inconel 718, and thus, the formation of the serrated chips involved. Evolution trends of the chip deformation results are of the main interest and focus is placed on the chip segmentation. It is shown that the simulation results of Inconel 718 can well agree with the available experiment or simulation results of many metals and alloys, as reported in the published literatures, due to the fact that these metals or alloys all involve shear localization leading to the serrated chip formation and thus show similar changes of chip pattern with the increase of cutting speed. Moreover, the FEM model is validated by comparing the chip morphologies from the experiments and the simulations, respectively.

The chip pattern of Inconel 718 is governed by various conditions, but largely depends on the cutting speed. At relatively low speeds, the continuously smooth chip forms. As the speed increases, a transition of chip form from the continuously smooth one to the serrated one appears. During the regularly serrated chip formation, the chip flow follows a repetitive pattern. Shear bands propagate through the entire chip thickness with regular spacing and without interactions between neighboring ones. But at high enough speeds, a totally different pattern of shear band emerges. It is observed that a family of shear bands is simultaneously growing within the primary shear zone. Most of the shear bands do not penetrate through the chip. The shear band spacings are irregular and so small that the shear bands can interact with each other before they are squeezed out of the chip formation region.

On the evolution, the finally equal limit of the primary shear angle ϕ_s and the segment inclination ϕ_{seg} is observed at very high cutting speeds. The segment inclination ϕ_{seg} results from the shear angle ϕ_s amplified by a compression process. Thus, ϕ_{seg} is generally greater than ϕ_s and gradually equal to ϕ_s. Indeed, it is observed that the

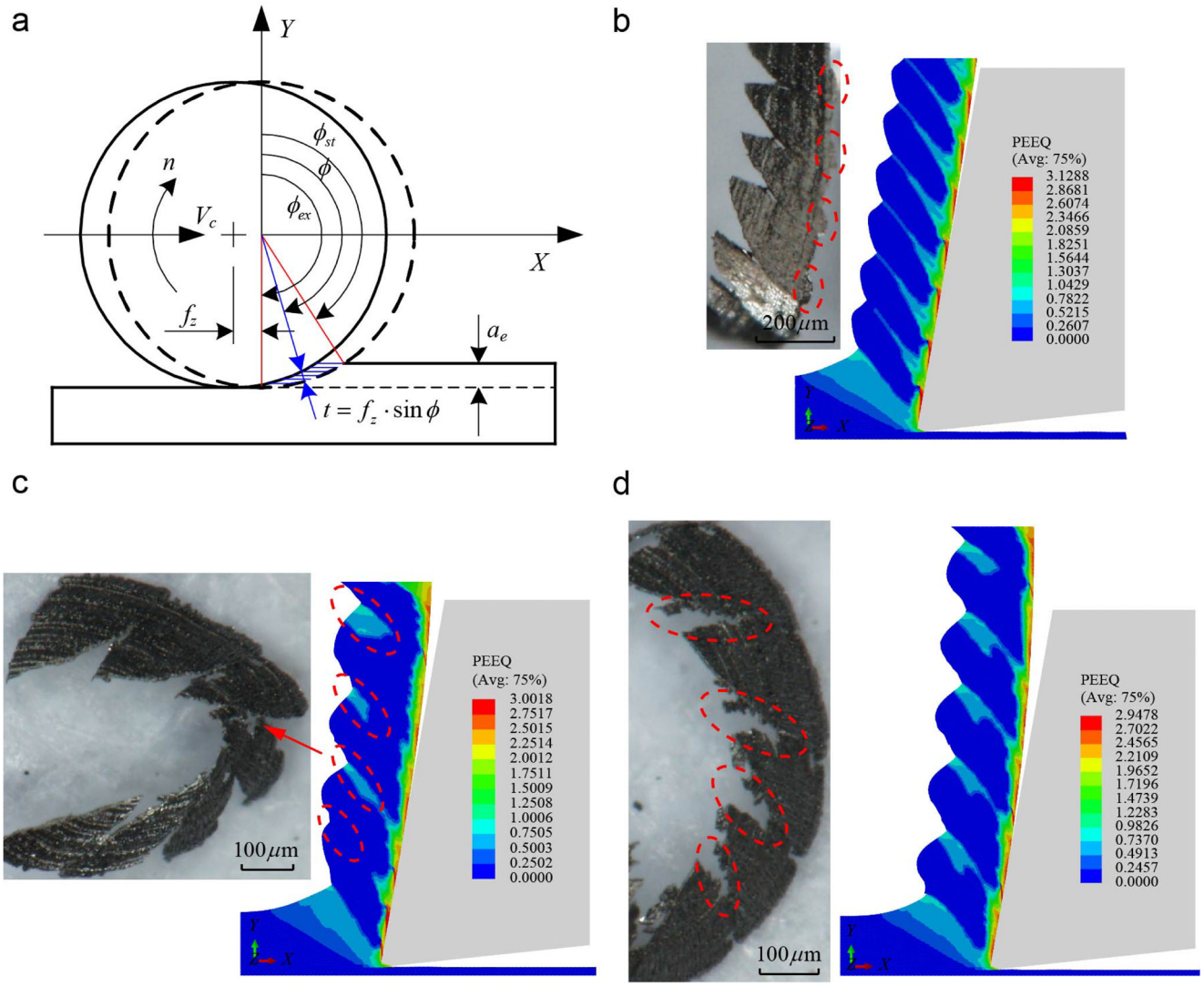

Fig. 19 The chip morphologies from milling experiments and corresponding simulations. **a** Sketch map of the milling process. **b** The cutting speed $V_c = 50$ m/min. **c** The cutting speed $V_c = 80$ m/min. **d** The cutting speed $V_c = 110$ m/min

segment inclination ϕ_{seg} decreases from a maximum value downwards to 45° at very high speeds, while the shear angle ϕ_s increases from a minimum value upwards to 45° eventually.

For the shear band spacing L_s or L_s/t_1, the transition to plateau regions is controlled by the subcritical speed V_{crit}^- and the supercritical speed V_{crit}^+, respectively. L_s reduces significantly as cutting speed approaching V_{crit}^- and exceeding V_{crit}^+. Based on the simulation results, the FEM simulations are applied to capture the two critical cutting speeds, at which the onset and the disappearance of chip serration (flow instability) occur. Therefore, it needs to qualify the values of V_{crit}^- and V_{crit}^+ as precise as possible. In addition, it is noted that V_{crit}^- is sensitive to the depth of cut, but V_{crit}^+ is almost insensitive to the depth of cut. It is also noted that L_s increases with the depth of cut. But in the plateau regions, it is seen that L_s/t_1 is nearly independent of the cutting speed and the depth of cut.

Heat transfer effect is embedded in the normalized cutting speed through the heat conductivity of workpiece material. It can be deduced that the heat conduction significantly affect the localized shear banding, especially the shear band spacing when cutting speed approaches V_{crit}^-. At relatively low cutting speeds, inertia effects play no role and can be neglected. The slow-down of cutting force could be explained by the predominance of thermal effects leading to adiabatic shear banding and material softening in the shear zones. With the increase of cutting speed, it is seen that the cutting force continuously increases. This is correlated with the inertia effects that start to become significant at high cutting speeds where the thermal effects do not have predominance. Inertia effects can also reduce

the intensity of chip serration and contribute to the increase of specific cutting force by parabolic growth. But the thermal effects and the inertia effects on shear band spacing are ineffective in the plateau regions. Altogether, the cutting force trend evaluated in the simulations is comparable to the published experiment results.

The cutting force frequency f_{force} and the chip segmentation frequency f_{seg} keep steps closely with each other as they evolve. Combined with the formation of successive shearing bands, it is concluded that the fluctuation of cutting force is closely associated with the chip segmentation. Furthermore, f_{force} and f_{seg} both linearly increase with the cutting speed when $V_c < V_{crit}^{+}$. However, they both witness an intense increase when $V_c > V_{crit}^{+}$. In the overall range of cutting speeds, there is a clearly linear relationship between the chip segmentation frequency f_{seg} and the cutting speed V_c in a log-log diagram. This tendency from simulations compares well with the published experimental measurements. It is also noticed that f_{seg} decreases with the increase of depth of cut.

It is seen that the segmentation degree D_s increases quickly in the early stage of cutting speed V_c, then reaches a saturation at intermediate stage of V_c and finally reduces and tends to zero at still higher V_c. However, when referring to the specific cutting force F_{ave}/t_1, it is seen that F_{ave}/t_1 in terms of V_c evolves contrarily when compared to the evolution of D_s. This makes sense since a higher value of D_s is associated with a higher intensity of shear strain localization and thus a higher temperature within the shear bands that will induce a decrease of cutting force by thermal softening happening in the shear zones.

Compared to the depth of cut, cutting speed seems to be a more important factor by affecting shear angle, shear band spacing, cutting force, segmentation frequency and chip serration intensity of Inconel 718. Very high cutting speed favors the expulsion of chip segmentation, and this can be confirmed by the decrease of segmentation degree. On the whole, the simulation results give clues to investigate the relationship of cutting speed and other correlated quantities in the chip formation process of Inconel 718, and it is fundamental to increase understandings of the alloy's machining characteristics and thus to push forward the study of difficult-to-cut metals and alloys with cutting speed increasing from low to very high range.

Acknowledgements The authors sincerely thanks to Mr. D. Y. Wen and Mr. H. Yuan for their critical discussion and reading during manuscript preparation.

Author contribution C. Liu wrote the manuscript, and was in charge of the simulation. M. Wan was in charge of the whole trial, review and edition. Y. Yang assisted with review. All authors read and approved the final manuscript.

Funding This research has been supported by the National Natural Science Foundation of China under Grant no. 51975481, and the Fundamental Research Funds for the Central Universities under Grant no. 3102020ZX004.

Declarations

Ethics approval The authors state that the present work is in compliance with the ethical standards.

Conflict of interests The authors declare no competing interests.

References

1. Thellaputta GR, Chandra PS, Rao CSP (2017) Machinability of nickel based superalloys: A review. Mater Today Proc 4(2):3712–3721
2. Rahman M, Seah WKH, Teo TT (1997) The machinability of Inconel 718. J Mater Process Technol 63(1):199–204
3. Pawade RS, Joshi SS, Brahmankar PK (2008) Effect of machining parameters and cutting edge geometry on surface integrity of high-speed turned Inconel 718. Int J Mach Tools Manuf 48(1):15–28
4. Vrabel M, Eckstein M, Mankova I (2018) Analysis of the metallography parameters and residual stress induced when producing bolt holes in Inconel 718 alloy. Int J Adv Manuf Technol 96(9-12):4353–4366
5. Ezugwu EO (2005) Key improvements in the machining of difficult-to-cut aerospace superalloys. Int J Mach Tools Manuf 45(12-13):1353–1367
6. Schulz H, Moriwaki T (1992) High-speed machining. CIRP Ann Manuf Technol 41(2):637–643
7. Thakur DG, Ramamoorthy B, Vijayaraghavan L (2009a) Study on the machinability characteristics of superalloy Inconel 718 during high speed turning. Mater Des 30(5):1718–1725
8. Sharman ARC, Hughes JI, Ridgway K (2004) Workpiece surface integrity and tool life issues when turning Inconel 718 nickel based superalloy. Mach Sci Technol 8(3):399–414
9. Liu C, Wan M, Zhang WH, Yang Y (2021) Chip formation mechanism of Inconel 718: a review of models and approaches. Chinese J Mechan Eng 34(1):34–49
10. Wang B, Liu ZQ, Yang QB (2013) Investigations of yield stress, fracture toughness, and energy distribution in high speed orthogonal cutting. Int J Mach Tools Manuf 73:1–8
11. Sutter G, List G (2013) Very high speed cutting of Ti-6Al-4V titanium alloy - change in morphology and mechanism of chip formation. Int J Mach Tools Manuf 66:37–43
12. Davies MA, Chou Y, Evans CJ (1996) On chip morphology, tool wear and cutting mechanics in finish hard turning. CIRP Ann 45(1):77–82
13. Tay AO, Stevenson MG, de Vahl Davis G (1974) Using the finite element method to determine temperature distributions in orthogonal machining. Proc Instit Mechan Eng 188(1):627–638
14. Ozel T, Llanos I, Soriano J, Arrazola PJ (2011) 3D finite element modelling of chip formation process for machining Inconel 718: comparison of FE software predictions. Machin Sci Technol 15(1):21–46
15. Semiatin SL, Rao SB (1983) Shear localization during metal cutting. Mater Sci Eng 61(2):185–192

16. Li GH, Wang MJ, Duan CZ (2009) Adiabatic shear critical condition in the high-speed cutting. J Mater Process Technol 209(3):1362–1367
17. Jawahir IS, van Luttervelt CA (1993) Recent developments in chip control research and applications. CIRP Ann Manuf Technol 42(2):659–693
18. Timothy SP, Hutchings IM (1985) The structure of adiabatic shear bands in a titanium alloy. Acta Metall 33(4):667–676
19. Komanduri R, Schroeder TA (1986) On shear instability in machining a nickel-iron base superalloy. J Eng Indust 108(2):93–100
20. Wright TW, Perzyna P (2003) Physics and mathematics of adiabatic shear bands. Appl Mech Rev 56(3):B41–B43
21. Zener C, Hollomon JH (1944) Effect of strain rate upon plastic flow of steel. J Appl Phys 15(1):22–32
22. Sutter G, Molinari A, List G, Bi X (2012) Chip flow and scaling laws in high speed metal cutting. J Manuf Sci Eng 134(2):021,005
23. Johnson GR, Cook WH (1985) Fracture characteristics of three metals subjected to various strains, strain rates, temperatures and pressures. Eng Fract Mech 21(1):31–48
24. Ye GG, Chen Y, Xue SF, Dai LH (2014) Critical cutting speed for onset of serrated chip flow in high speed machining. Int J Mach Tools Manuf 86:18–33
25. Atlati S, Haddag B, Nouari M, Zenasni M (2011) Analysis of a new segmentation intensity ratio "SIR" to characterize the chip segmentation process in machining ductile metals. Int J Mach Tools Manuf 51(9):687–700
26. Yong Y, Ying-lin K, Hui-yue D (2006) Finite element simulation of high-speed cutting. Acta Aeronauticaet Astronautica Sinica 27(3):531–535
27. Komvopoulos K, Erpenbeck SA (1991) Finite element modeling of orthogonal metal cutting. J Eng Indust 113(3):253–267
28. Hillerborg A, Modeer M, Petersson PE (1976) Analysis of crack formation and crack growth in concrete by means of fracture mechanics and finite elements. Cem Concr Res 6(6):773–781
29. Bao Y, Wierzbicki T (2004) On fracture locus in the equivalent strain and stress triaxiality space. Int J Mech Sci 46(1):81–89
30. Strenkowski JS, Carroll JT (1985) A finite element model of orthogonal metal cutting. J Eng Indust 107(4):349–354
31. Rusinek A, Zaera R (2007) Finite element simulation of steel ring fragmentation under radial expansion. Int J Impact Eng 34(4):799–822
32. Rodriguez-Martinez JA, Vadillo G, Fernandez-Saez J, Molinari A (2013) Identification of the critical wavelength responsible for the fragmentation of ductile rings expanding at very high strain rates. J Mechan Phys Solids 61(6):1357–1376
33. Molinari A, Soldani X, Miguelez MH (2013) Adiabatic shear banding and scaling laws in chip formation with application to cutting of Ti-6Al-4V. J Mechan Phys Solids 61(11):2331–2359
34. Molinari A, Cheriguene R, Miguelez H (2011) Numerical and analytical modeling of orthogonal cutting: The link between local variables and global contact characteristics. Int J Mech Sci 53(3):183–206
35. Hortig C, Svendsen B (2007) Simulation of chip formation during high-speed cutting. J Mater Process Technol 186(1-3):66–76
36. Soldani X, Santiuste C, Munoz-Sanchez A, Miguelez MH (2011) Influence of tool geometry and numerical parameters when modeling orthogonal cutting of LFRP composites. Compos A: Appl Sci Manuf 42(9):1205–1216
37. Soldani X, Munoz-Sanchez A, Miguelez H, Molinari A (2010) Numerical modeling of segmentation phenomenon in orthogonal cutting. Proceedings of the 2nd CIRP International Conference Process Machine Interactions, Vancouver, Canada
38. Komanduri R, Brown RH (1981) On the mechanics of chip segmentation in machining. J Eng Indust 103(1):33–51
39. Vyas A, Shaw MC (1999) Mechanics of saw-tooth chip formation in metal cutting. J Manuf Sci Eng 121(2):163–172
40. Ozel T, Ulutan D (2013) Effects of machining parameters and tool geometry on serrated chip formation, specific forces and energies in orthogonal cutting of nickel-based super alloy Inconel 100. Proc Instit Mechan Eng Part B J Eng Manuf 228(7):673–686
41. Molinari A, Musquar C, Sutter G (2002) Adiabatic shear banding in high speed machining of ti-6al-4v: experiments and modeling. Int J Plast 18(4):443–459
42. Wang B, Liu ZQ, Song QH, Wan Y, Ren XP (2020) An approach for reducing cutting energy consumption with ultra-high speed machining of super alloy Inconel 718. Int J Precis Eng Manuf - Green Technol 7:35–51
43. Flom DG, Komanduri R, Lee M (1984) High-speed machining of metals. Annu Rev Mater Sci 14(1):231–278
44. Merchant ME (1945) Mechanics of the metal cutting process. i. orthogonal cutting and a type 2 chip. J Appl Phys 16(5):267–275
45. Sutter G (2005) Chip geometries during high-speed machining for orthogonal cutting conditions. Int J Mach Tools Manuf 45(6):719–726
46. Ye GG, Xue SF, Jiang MQ, Tong XH, Dai LH (2013) Modeling periodic adiabatic shear band evolution during high speed machining Ti-6Al-4V alloy. Int J Plast 40:39–55
47. Cai SL, Dai LH (2014) Suppression of repeated adiabatic shear banding by dynamic large strain extrusion machining. J Mechan Phys Solids 73:84–102
48. Arunachalam RM, Mannan MA, Spowage AC (2004) Surface integrity when machining age hardened Inconel 718 with coated carbide cutting tools. Int J Mach Tools Manuf 44(14):1481–1491
49. Toenshoff HK, Winkleri H, Patzke M (1984) Chip formation at high-cutting speeds. American Society of Mechanical Engineers, Production Engineering Division
50. Bonnet-Lebouvier AS, Molinari A, Lipinski P (2002) Analysis of the dynamic propagation of adiabatic shear bands. Int J Solids Struct 39(16):4249–4269
51. Wright TW, Ockendon H (1996) A scaling law for the effect of inertia on the formation of adiabatic shear bands. Int J Plast 12(7):927–934
52. Molinari A (1997) Collective behavior and spacing of adiabatic shear bands. J Mechan Phys Solids 45(9):1551–1575
53. Barry J, Byrne G, Lennon D (2001) Observations on chip formation and acoustic emission in machining Ti-6Al-4V alloy. Int J Mach Tools Manuf 41(7):1055–1070
54. Duan CZ, Zhang LC (2012) Adiabatic shear banding in AISI 1045 steel during high speed machining: mechanisms of microstructural evolution. Mater Sci Eng A 532:111–119
55. Chuzhoy L, DeVor RE, Kapoor SG (2003) Machining simulation of ductile iron and its constituents, part 2:, numerical simulation and experimental validation of machining. J Manuf Sci Eng 125(2):192–201
56. Cotterell M, Byrne G (2008) Dynamics of chip formation during orthogonal cutting of titanium alloy Ti-6Al-4V. CIRP Ann Manuf Technol 57(1):93–96
57. Yang QB, Wu Y, Liu D, Chen L, Lou DY, Zhai ZS, Liu ZQ (2016) Characteristics of serrated chip formation in high-speed machining of metallic materials. Int J Adv Manuf Technol 86(5-8):1201–1206
58. Ye GG, Jiang MQ, Xue SF, Ma W, Dai LH (2018) On the instability of chip flow in high-speed machining. Mech Mater 116:104–119

59. Larbi S (1990) Contribution à l'étude de l'usinage à grandes vitesses de matériaux métalliques par simulation sur un banc d'essai à base de barres de hopkinson thèse de Doctorat, Université de Nantes, France
60. Hoffmeister HW, Gente A, Weber TH (1999) Chip formation at titanium alloys under cutting speed of up to 100 m/s. In: 2nd International Conference on High Speed Machining, PTW Darmstadt University, pp 21–28
61. Dudzinski D, Molinari A (1997) A modelling of cutting for viscoplastic materials. Int J Mech Sci 39(4):369–389
62. Recht RF (1985) A dynamic analysis of high-speed machining. J Eng Indust 107(4):309–315
63. Arndt G (1973) Ultra-high-speed machining: a review and an analysis of cutting forces. Proc Instit Mechan Eng 187(1):625–634
64. Klocke F, Raedt HW, Hoppe S (2001) 2D-FEM simulation of the orthogonal high speed cutting process. Machin Sci Technol An Int J 5(3):323–340
65. Baker M (2006) Finite element simulation of high-speed cutting forces. J Mater Process Technol 176(1-3):117–126
66. Schulz H, Abele E, Sahm A (2001) Material aspects of chip formation in HSC machining. CIRP Ann Manuf Technol 50(1):45–48
67. Wang B, Liu ZQ (2014) Serrated chip formation mechanism based on mixed mode of ductile fracture and adiabatic shear. Proc Instit Mechan Eng Part B J Eng Manuf 228(2):181–190
68. Su GS, Liu ZQ, Li L, Wang B (2015) Influences of chip serration on micro-topography of machined surface in high-speed cutting. Int J Mach Tools Manuf 89:202–207
69. Wang B, Liu ZQ (2015) Shear localization sensitivity analysis for Johnson-Cook constitutive parameters on serrated chips in high speed machining of Ti6Al4V. Simul Model Pract Theory 55:63–76
70. Thakur DG, Ramamoorthy B, Vijayaraghavan L (2009b) A study on the parameters in high-speed turning of superalloy Inconel 718. Mater Manuf Process 24(4):497–503
71. Komanduri R (1982) Some clarifications on the mechanics of chip formation when machining titanium alloys. Wear 76(1):15–34
72. Altintas Y (2012) Manufacturing automation: metal cutting mechanics, machine tool vibrations, and CNC design. Cambridge University Press, Cambridge